CONCEPT FOR ROOM TEMPERATURE SINGLE-SPIN TUNNELING FORCE MICROSCOPY WITH ATOMIC SPATIAL RESOLUTION

by

Adam Payne

A dissertation submitted to the faculty of
The University of Utah
in partial fulfillment of the requirements for the degree of

Doctor of Philosophy

in

Physics

Department of Physics and Astronomy

The University of Utah

December 2015

The University of Utah Graduate School

STATEMENT OF DISSERTATION APPROVAL

The dissertation of **Adam Payne**

has been approved by the following supervisory committee members:

Clayton Williams	, Chair	**6/23/15** Date Approved
Scott Anderson	, Member	**6/23/15** Date Approved
Christoph Boehme	, Member	**06/23/15** Date Approved
Stephane LeBohec	, Member	**06/24/15** Date Approved
Eugene Mishchenko	, Member	**06/24/15** Date Approved

and by **Carleton DeTar** , Chair/Dean of

the Department/College/School of **Physics and Astronomy**

and by David B. Kieda, Dean of The Graduate School.

ABSTRACT

A study of a force detected single-spin magnetic resonance measurement concept with atomic spatial resolution is presented. The method is based upon electrostatic force detection of spin-selection rule controlled single electron tunneling between two electrically isolated paramagnetic states. Single-spin magnetic resonance detection is possible by measuring the force detected tunneling charge noise on and off spin resonance. Simulation results of this charge noise, based upon physical models of the tunneling and spin physics, are directly compared to measured atomic force microscopy (AFM) system noise. The results show that the approach could provide single-spin measurement of electrically isolated defect states with atomic spatial resolution at room temperature.

To my wife Heather… for her support, patience and love.

TABLE OF CONTENTS

LIST OF FIGURES

Figure

ACKNOWLEDGMENTS

I would like to thank Clayton Williams for the many years of collaboration, encouragement and guidance. His discernment for knowing when to help and when to let go was crucial in helping me develop the critical thinking skills that I needed. Jon Johnson, Dustin Winslow and Philipp Rahe taught me the subtleties of atomic force microscopy and ultra-high vacuum and patiently answered all my questions, no matter how many times I repeated them. I will miss the long discussions and helpful collaboration with Kapildeb Ambal. His friendship and professional advice were invaluable.

Finally, none of this would be possible without the support of my wife Heather and my children: Conner, Lucas and Hannah. On good days and bad days, I always came home to people who loved me with open arms. I cannot sufficiently express the foundational role they have played in my life's happiness.

CHAPTER 1

INTRODUCTION TO SINGLE-SPIN MEASUREMENTS

Background and Motivation

Since the 1960s, the semiconductor industry has used Moore's Law[1] as a long-term guide for planning its next generation of computer processors. A number of improvements in semiconductor processes have allowed engineers and scientists to double the number of transistors roughly every two years. Zhirnov et al.[2] hypothesized in 2005 that challenges would limit processing technology to 16 nm and that gate oxides could be minimized to a limit of 5 nm due to quantum mechanical effects. Since that prediction, high-k dielectrics have been used to produce 1 nm equivalent gate oxide thickness for 45 nm processing technologies, showing that seemingly unsurmountable challenges can sometimes be overcome. Still, there is a growing field of engineers and scientists trying to develop alternative paths, including quantum computing approaches, in order to expand future computational opportunities.

Semiconductor materials are well known to contain paramagnetic defects whose properties could be used as the coherent qubits needed for quantum computation.[3, 4] These qubits benefit by being electrically isolated to mitigate sources of decoherence.[5] They could potentially be addressable with techniques that have single-spin sensitivity and atomic scale spatial resolution. A conceptual approach for the use of individual spins in quantum computational devices has been proposed[6, 7] by Kane et al. where a silicon based,

single-spin detection and readout scheme uses nuclear spins located in donor atoms. For decades, magnetic resonance techniques have been used in detecting and understanding the spin signatures found in various materials and the spin detection sensitivity of these techniques has continuously improved. In 1993, Wrachtrup et al. successfully detected magnetic resonance in a single pentacene molecule by combining single molecule fluorescence spectroscopy and optically detected magnetic resonance (ODMR).[8] Since that first single-spin detection experiment, various methods have been employed to increase the spatial resolution of single-spin detection. Spatially well-defined single-spin readout utilizing spin-selection rules has been demonstrated in the past on electronic transitions between double charge quantum dots.[9-11] Other methods include various electrical[12-14] readout techniques (the spatial resolution is limited by the size of the device, ~1 μm^2), and optical techniques (i.e., detecting the fluorescence of individual defect centers in diamond with 330 nm spatial resolution, using a scanning confocal optical microscope[15]). Although magnetic force detection, a scanning probe based technique,[16-18] has achieved spatial resolution of ~25 nm, detection of single spins require significant signal averaging of up to 13 hours/point. Therefore, despite these advancements, experimentally demonstrated single-spin detection of individual, isolated paramagnetic point defects still has spatial resolutions one to two orders of magnitude above the localization of the paramagnetic states.[8, 12, 14, 16] This limitation makes the application of these spin measurement techniques for a selective readout of adjacent paramagnetic states difficult – or, as recently demonstrated, they are based on either scanning tunneling microscopy (STM),[19] spin-polarized scanning tunneling microscopy, [20, 21] or magnetic exchange force microscopy,[21, 22,23] all of which employ conductive probe tips, with free

carriers that could limit spin coherence times of qubits when the spin readout is used for quantum information applications. Thus, a reliable single-spin detection technique with atomic resolution and access to isolated paramagnetic states is still needed.

In recent years, individual electronic tunneling events have been observed by single electron tunneling force microscopy (SETFM), which is based on the detection of electrostatic forces caused by single electron tunneling between electronic point defects and a *conducting* atomic force microscopy (AFM) cantilever probe[24]. Its capabilities for single electron tunneling spectroscopy, 3D imaging, and quantum state energy depth measurement on the atomic length scale have been well demonstrated.[25-31] Since this method relies on electrostatic force detection of individual tunneling events, it works with surfaces that allow paramagnetic states to be completely electrically isolated and, therefore allows potentially long spin coherence times suitable for quantum information applications. Because the probe tip is metallic, however, this technique (SETFM) is insensitive to spin selection rules and, therefore can only observe charge, and *not spin.*

This work presents a theoretical feasibility study of a scanning probe based, single-spin detection scheme, with atomic scale spatial resolution. It is based on electrostatic force detection of spin-selection rule controlled single electron tunneling. Because the methodology and analysis uses electrostatic force detection of individual tunneling events, two important advantages are achieved: it avoids a conducting substrate that inhibits long spin coherence times and it allows atomic spatial resolution based on the previous work of single electron tunneling force microscopy.[24, 25] Specifically, single electron tunneling, between two paramagnetic states (one in a non-conducting substrate and the other at the apex of a non-conducting AFM probe tip) produces a random telegraph signal (RTS) which

is detected by a non-contact atomic force microscope. Chapter 2 outlines the computational algorithm and simulates the tunneling RTS for 3 scenarios: tunneling only, off magnetic resonance, and on magnetic resonance. The tunneling RTS is then analyzed in the presence of a finite detection bandwidth. Chapter 3 describes how the force gradient produced by the tunneling RTS is converted into a cantilever frequency shift. This is used to scale the simulation output to a measureable frequency shift. The parameters of an E' center (a common defect found in thermal oxides) are used in the RTS simulation (T_1 process) and the electrostatic model (coulomb energy). The simulation and electrostatic model show that the E' center is a good candidate defect for the proposed experiment. Chapter 4 details optimizations to an existing commercial AFM under ultra-high vacuum (UHV) and describes subsequent measurements of the AFM system noise in the presence of tip sample interactions. These system noise measurements are necessary in order to show that the single-spin tunneling force detection scheme is viable at room temperature for an E' center type system. Chapter 5 describes a random telegraph signal experimentally observed on an atomic force microscope at the University of Utah. This signal was measured to determine if it behaved like the theoretical tunneling RTS model predictions and to clarify its suitability in the single-spin tunneling force experiment. It concludes with a summary of the work and future outlook.

References

1. G. E. Moore, Electronics **38,** 114 (1965).

2. V. V. Zhirnov, R. K. Cavin, J. A. Hutchby, and G. I. Bourianoff, Proc. IEEE **91**, 1934 (2003).

3. K. Saeedi, S. Simmons, J. Z. Salvail, P. Dluhy, H. Riemann, N. V. Abrosimov, P. Becker, H.-J. Pohl, J. J. L. Morton, and M. L. W. Thewalt, Science **342**, 830 (2013).

4. P. C. Maurer, G. Kucsko, C. Latta, L. Jiang, N. Y. Yao, S. D. Bennett, F. Pastawski, D. Hunger, N. Chisholm, M. Markham, D. J. Twitchen, J. I. Cirac, and M. D. Lukin, Science **336**, 1283 (2012).

5. D. P. DiVincenzo, Science **270**, 255 (1995).

6. B. E. Kane, Nature **393**, 133 (1998).

7. C. Boehme and K. Lips, Phys. Status Solidi B **233**, 427 (2002).

8. J. Wrachtrup, C. von Borczyskowski, J. Bernard, M. Orritt, and R. Brown, Nature **363**, 244 (1993).

9. A. C. Johnson, J. R. Petta, J. M. Taylor, A. Yacoby, M. D. Lukin, C. M. Marcus, M. P. Hanson, and A. C. Gossard, Nature **435**, 925 (2005).

10. J. R. Petta, A. C. Johnson, J. M. Taylor, E. A. Laird, A. Yacoby, M. D. Lukin, C. M. Marcus, M. P. Hanson, and A. C. Gossard, Science **309**, 2180 (2005).

11. J. R. Prance, Z. Shi, C. B. Simmons, D. E. Savage, M. G. Lagally, L. R. Schreiber, L. M. K. Vandersypen, M. Friesen, R. Joynt, S. N. Coppersmith, and M. A. Eriksson, Phys. Rev. Lett. **108**, 046808 (2012).

12. A. Morello, J. J. Pla, F. A. Zwanenburg, K. W. Chan, K. Y. Tan, H. Huebl, M. Mottonen, C. D. Nugroho, C. Yang, J. A. van Donkelaar, A. D. C. Alves, D. N. Jamieson, C. C. Escott, L. C. L. Hollenberg, R. G. Clark, and A. S. Dzurak, Nature **467**, 687 (2010).

13. J. M. Elzerman, R. Hanson, L. H. Willems van Beveren, B. Witkamp, L. M. K. Vandersypen, and L. P. Kouwenhoven, Nature **430**, 431 (2004).

14. M. Xiao, I. Martin, E. Yablonovitch, and H. W. Jiang, Nature **430**, 435 (2004).

15. A. Gruber, A. Dräbenstedt, C. Tietz, L. Fleury, J. Wrachtrup, and C. v. Borczyskowski, Science **276**, 2012 (1997).

16. D. Rugar, R. Budakian, H. J. Mamin, and B. W. Chui, Nature **430**, 329 (2004).

17. H. J. Mamin, M. Kim, M. H. Sherwood, C. T. Rettner, K. Ohno, D. D. Awschalom,

and D. Rugar, Science **339**, 557 (2013).

18. S. Müllegger, S. Tebi, A. K. Das, W. Schöfberger, F. Faschinger, and R. Koch, Phys. Rev. Lett. **113**, 133001 (2014).

19. S. Müllegger, S. Tebi, A. K. Das, W. Schöfberger, F. Faschinger, and R. Koch, Phys. Rev. Lett. **113**, 13 (2014).

20. R. Wiesendanger, I. V. Shvets, D. Bürgler, G. Tarrach, H. J. Güntherodt, J. M. D. Coey, and S. Gräser, Science **255**, 583 (1992).

21. R. Wiesendanger, Rev. Mod. Phys. **81**, 1495 (2009).

22. U. Kaiser, A. Schwarz, and R. Wiesendanger, Nature **446**, 522 (2007).

23. F. Pielmeier and F. J. Giessibl, Phys. Rev. Lett. **110**, 266101 (2013).

24. E. Bussmann, D. J. Kim, and C. C. Williams, Appl. Phys. Lett. **85**, 2538 (2004).

25. E. Bussmann and C. C. Williams, Appl. Phys. Lett. **88**, 263108 (2006).

26. J. P. Johnson, N. Zheng, and C. C. Williams, Nanotechnology **20**, 055701 (2009).

27. C. C. Williams, in *Fundamentals of Picoscience* (Taylor and Francis Group, LLC, Boca Raton, Florida, 2013), pp. 195.

28. J. P. Johnson, D. W. Winslow, and C. C. Williams, Appl. Phys. Lett. **98**, 052902 (2011).

29. D. Winslow and C. Williams, J. Appl. Phys. **110**, 114102 (2011).

30. D. W. Winslow, J. P. Johnson, and C. C. Williams, Appl. Phys. Lett. **98**, 172903 (2011).

31. R. Wang, S. W. King, and C. C. Williams, Appl. Phys. Lett. **105**, 052903 (2014).

CHAPTER 2

SIMULATING A TUNNELING RANDOM TELEGRAPH SIGNAL

Tunneling RTS Simulation Model

Probability Distribution of Tunneling Times and Spin Flip Times

In general, a random telegraph signal (RTS) is a stochastic process (memoryless and continuous in time) that shows two distinct values. The RTS considered here is governed primarily by two different, simultaneous quantum processes. The first is an electron tunneling through the vacuum gap, back and forth between two paramagnetic states, one in the tip oxide and the other in the sample oxide. This process is random and the tunneling rate depends on the size of the tunneling energy barrier height and its width.[1] For a given tunneling barrier, the electron tunneling can be characterized by an average tunneling time T_t, which is the average time the electron stays in the tip state before it tunnels to the sample, or vice versa. The second random process is the spin flipping of either of the electrons. The state will change its spin orientation after some time of interacting with its environment and this process is characterized by a spin lattice relaxation time T_1. Figure 1a) illustrates the two different quantum processes that determine the tunneling RTS. Figure 1b) shows the three possible charge and spin configurations that the system can have while T_1 processes and tunneling processes occur simultaneously. Both the tunneling and spin flipping are stochastic processes and obey Poisonian statistics.[2] Each has exponentially decaying probability distributions according to the formula,

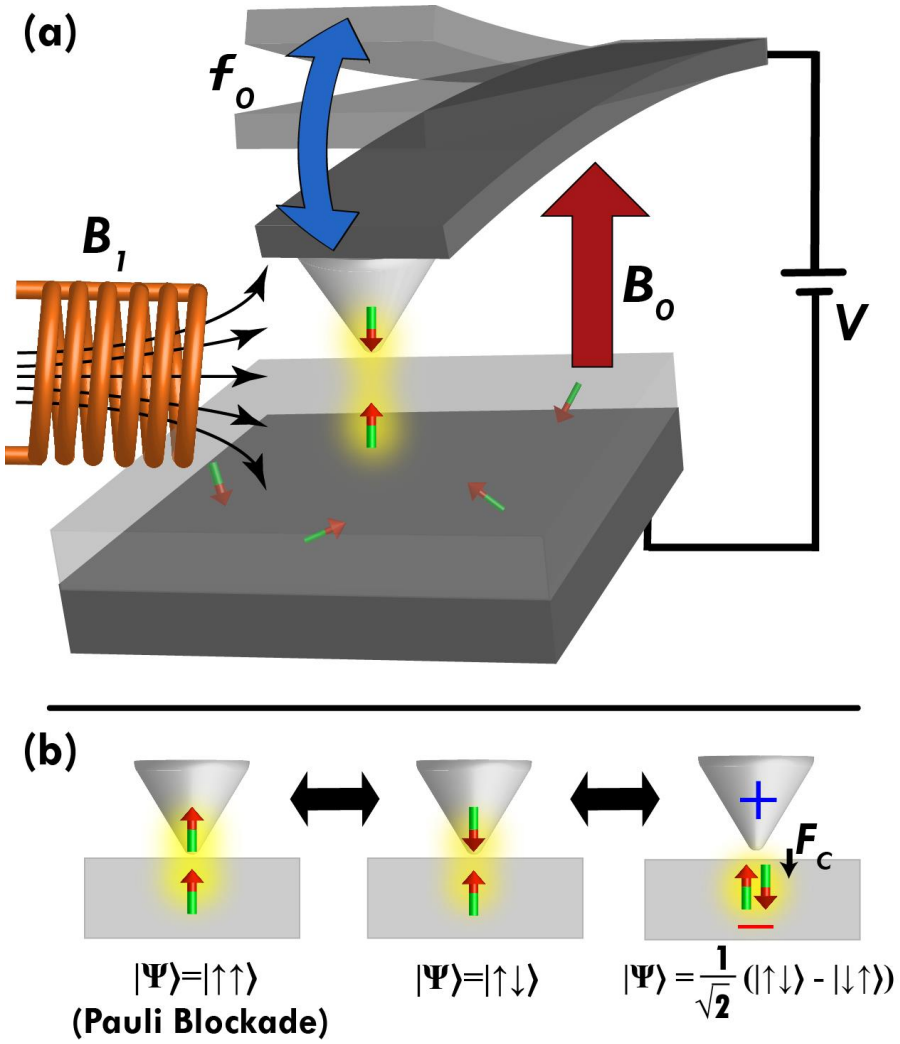

Figure 1: Illustration of the proposed electrostatic force detected single-spin microscope concept (a) Electrostatic force detected single-spin microscope consisting of a scanning probe setup that includes a cantilever with a paramagnetic state at its tip, a paramagnetic state at the sample and a magnetic resonance setup (rf and dc magnetic fields). (b) Illustrations of three possible charge and spin configurations of the probe-spin/test-spin pair. Left: High triplet content when Pauli exclusion prohibits tunneling, but spin-lattice relaxation allows for spin transitions towards mixed singlet/triplet states. Center: Spin pair states with mixed symmetry which allows for tunneling. Right: Tunneling creates a doubly occupied diamagnetic singlet state where both the cantilever and the surface contain opposite charge whose net force gradient results in a cantilever frequency shift.

$$P(t) = \frac{e^{\frac{-t}{\tau}}}{\tau} \quad (1)$$

where t is time, τ is the average time (either T_t or T_1) and P(t) is the probability that an event (tunneling or spin flipping) happens at time t. Equation (1) is used in the simulation, along with a random number generator to calculate random tunneling and spin flip times based upon this probability distribution with an average tunneling time/flip time of either T_t or T_1. Figure 2 shows a histogram of randomly generated tunneling times based on a Matlab program with a random number generator that follows the probability distribution in Equation (1).

The red curve represents the probability predicted by Equation (1) with $\tau = T_t = 1$ ms. The green bar is the average of the generated tunneling times. The average simulated tunneling time agrees with the theoretical average $T_t = 1$ ms.

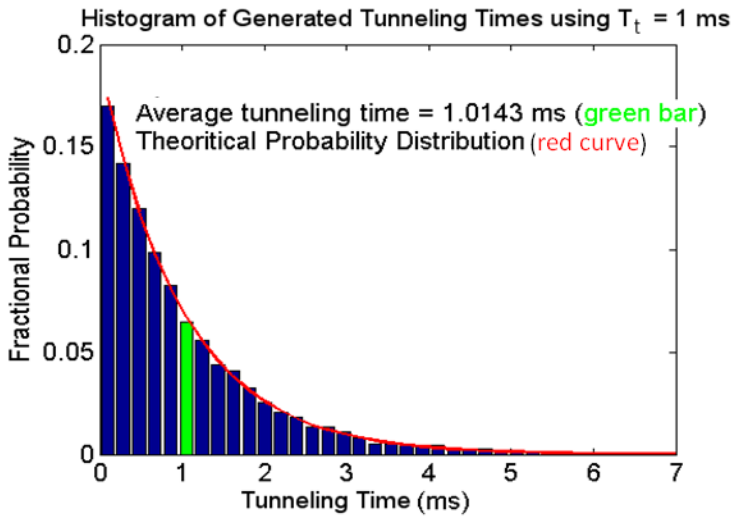

Figure 2: Histogram of randomly generated tunneling times produced in Matlab with a theoretical average T_t value of 1 ms. The red curve comes from the theoretical probability distribution (Poissonian) and the green bar is the average tunneling time that comes from the histogram of generated tunneling times.

Tunneling RTS Simulation Algorithm

Using the probability distribution described in Figure 2, with average tunneling time T_t and average flip time T_1, a computer simulation was written to simulate the tunneling RTS signal in the presence of spin flipping. Figure 3 shows a programming flow diagram of the tunneling RTS simulation.

In the algorithm, the electrons are initially separated (one in the tip and the other in the sample) and their relative spin orientation is antiparallel. At this point, the electron in the tip has two options:

a) Tunnel to the surface and after some time tunnel back to the tip, or

b) Flip its spin orientation while in the tip and after some time flip it back.

Note that if the electron flips its spin orientation while in the tip, it can no longer tunnel to the surface due to the Pauli-exclusion principle because its spin is parallel to the spin of the sample electron.

To begin the simulation, with the electrons separated and antiparallel, the code randomly generates both a tunneling time t_t and a flip time t_f. If $t_t < t_f$ (1^{st} possibility), the electron in the tip tunnels to the state at the surface after a time t_t. While the electrons are together, their relative spin orientations cannot change. Therefore a new t_t is randomly generated and the electron tunnels back to the tip state at that time. If $t_t > t_f$ (2^{nd} possibility), the electron in the tip will flip its spin orientation after a time t_f. At this point, the tip electron and sample electron have a parallel spin orientation and so tunneling is prohibited. A new t_f is then randomly generated. The electron randomly flips its orientation back to an antiparallel state at that time t_f, after which future tunneling can occur, and the process starts over.

At each step of the algorithm, the relative location and relative spin orientation of

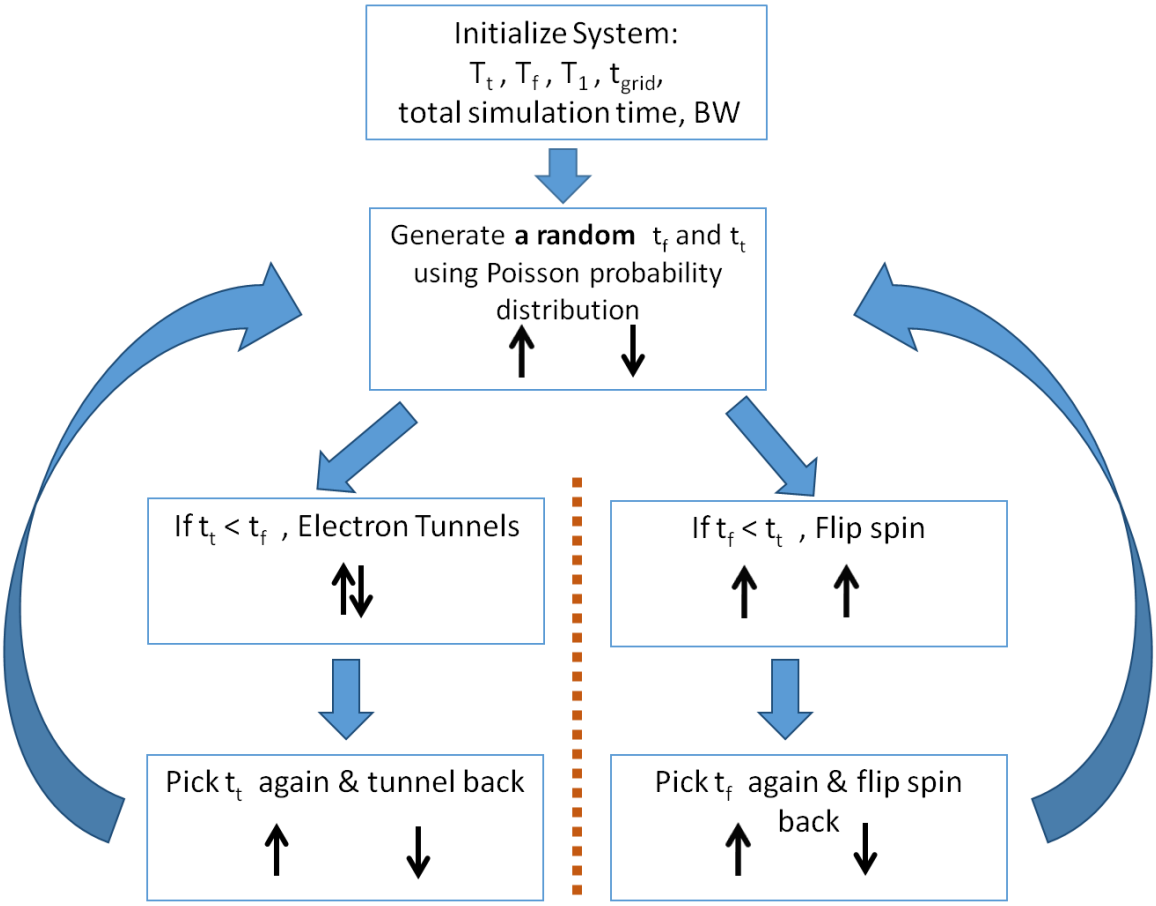

Figure 3: Tunneling RTS schematic algorithm. Tunneling times and spin flip times are generated using their respective Poissonian distribution and used in the above algorithm to simulate the spin dependent tunneling RTS. The times are recorded on a fine time grid of resolution t_{grid}.

the electrons are recorded using a fine time grid. The fine grid time step is chosen to be small compared to all of the processes of interest. For most simulations, the average T_t = 10 μs, the fine grid spacing is 100 ns and the simulation is run for a total time of 1 second.

Simulating On and Off Resonance Effects

In the proposed experiment, as the electron tunnels back and forth between the sample and the tip, electron spin resonance (ESR) driving fields (static and rf magnetic fields) are applied. When the frequency of the rf magnetic field matches the natural precision frequency of the electron in the tip, the magnetic resonance condition is met, and

the applied field can flip its spin orientation. Because the sample and tip electron will have slightly different g-factors, we assume that only the tip electron is in magnetic resonance. If the rf field strength is large enough (and on resonance), the separated sample spin can flip relative to the probe spin on a time scale that is fast compared to the intrinsic T_1 spin flip time. This decreases the time that spin blocking occurs and effectively shortens the spin lattice relaxation time from T_1 to the B_1 driven average spin flip rate ($T_{1res} = \gamma B_1$ when the field is tuned to resonance). Thus, the applied rf field reduces the average time interval that the electrons are separated and spin blocked. It is important to note that the individual driven spin flips are still stochastic in nature and still follow the probability distribution discussed earlier, but simply with a smaller "effective" T_1 parameter. The average tunneling time T_t does not change when magnetic resonance is achieved, since it is determined only by the tunneling barrier.

Filtering

In recording the relative position of the electrons, ones and zeros are used to identify the electrons as separated and together respectively. For the relative spin alignment, the antiparallel and parallel spin states are assigned -1 and 1 respectively. These designations make step like transitions in the time domain simulations, which corresponds to having an infinite amount of detection bandwidth in the actual experiment. In order to better simulate the experimental results, which have a finite amount of measurement bandwidth, the simulation output is filtered with a numerical first-order low-pass filter. The low-pass filter, seen in Equation (2), has a transfer function,

$$G_{low}^2(\omega) = \frac{1}{1 + \frac{f^2}{f_{lc}^2}} \qquad (2)$$

In this equation, f_{lc} is the low-pass cut-off frequency.

Computational Output Analysis

Random Telegraph Signal

Figure 4 shows the results from a tunneling RTS simulation. The three graphs on the left hand side were produced with $T_1 >> T_t$. This condition makes it very improbable that a random spin flip occurs compared to a tunneling event. The middle left graph shows an electron tunneling back and forth between the tip and the sample with an average tunneling time T_t = 10 μs and T_1 = 1 second. The regions that appear as a solid color are actually multiple tunneling events that can be seen in the top left graph of Figure 4. No spin flip events occur during this time. The bottom left graph shows that the spin orientation remains constant.

The three graphs on the right hand side were produced with T_1 = 200 μs and T_t = 10 μs, showing simulation results in which both electron tunneling and spin flipping occur. When the spins are aligned antiparallel (denoted as "-1" in the bottom right graph), the electron is able to tunnel back and forth between the tip and the sample (middle right graph and also zoomed version in the top right graph) at the average tunneling rate of T_t. When the spins are aligned parallel (denoted as "1" in the bottom right graph), which can only occur when they are separated, there are no tunneling events due to the spin blockade for a time which is on average T_1. This may be referred to as "blinking". The bottom right graph shows the relative spin orientation changing, on average, after a spin lattice relaxation time of T_1 = 200 μs

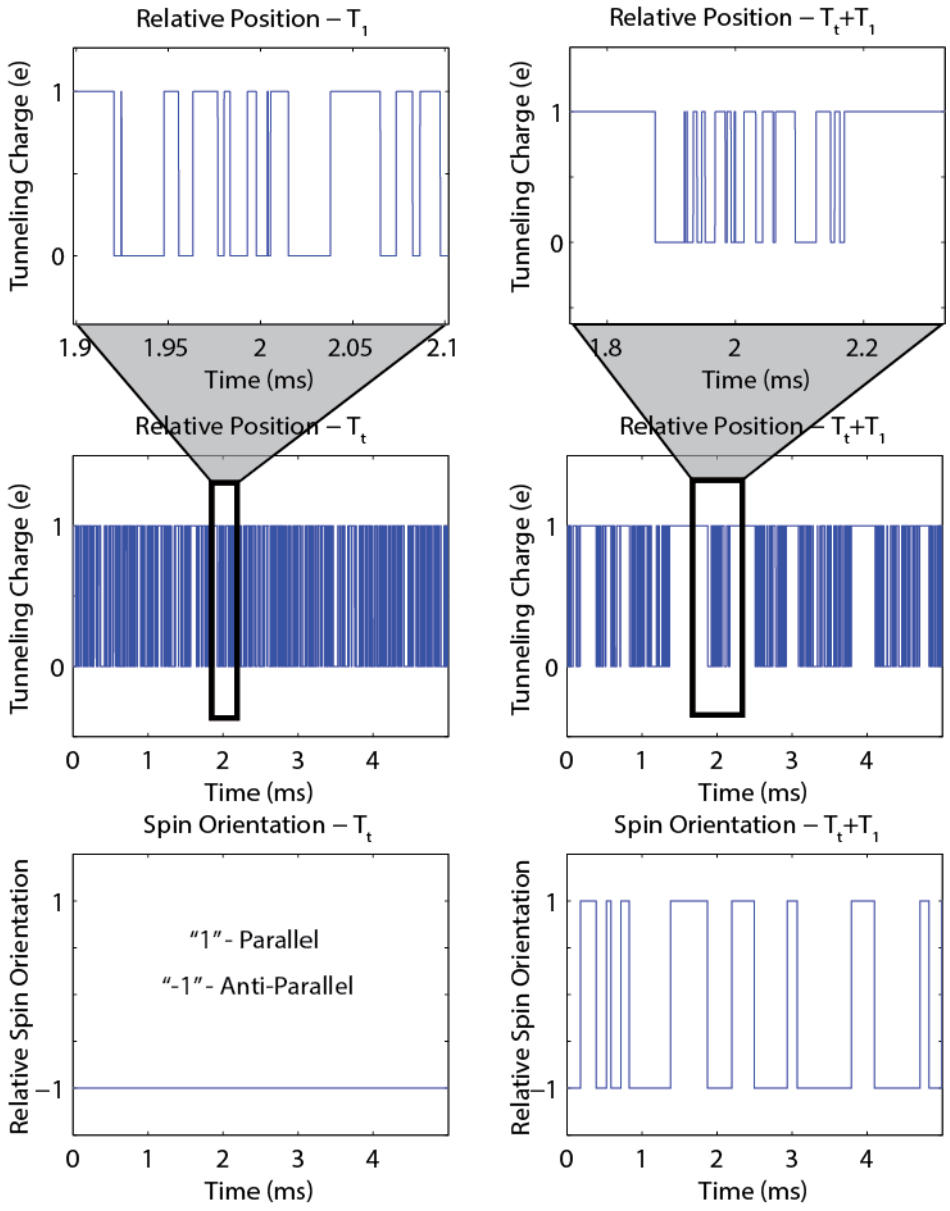

Figure 4: Tunneling RTS – time domain. Top two rows show the tunneling charge in the time domain. Top row shows a zoomed in portion of the tunneling charge in the second row. The bottom row graphs are the relative spin orientation.

Lorentzian Power Spectrum

It can be shown that the power spectrum of the observed random telegraph signal (one without spin blockades) is Lorentzian[2] according to Equation (3),

$$S = \frac{2e^2 T_t}{4 + 4\pi^2 f^2 T_t^2} \quad (3)$$

where S is the power spectral density, T_t is the average tunneling time in seconds, and *f* is the frequency in Hertz. Figure 5 shows the power spectral density (on a log-log plot) for a tunneling RTS simulation with T_t = 1 ms and total simulation time of 1 second, without any spin blockade. The black curve is the theoretical power spectral density from Equation (3) and the yellow portion is the power spectrum of the tunneling RTS simulation showing nice agreement. The tunneling RTS power spectrum is achieved by squaring the absolute value of the Fourier transform from the tunneling RTS time domain data.

The graph shows that at large frequencies, the power spectrum falls off as f^{-2}. At low frequency, the spectrum is constant. Finally, the roll-off frequency of the data is close to the value of $2/T_t$ radians as expected. These characteristics in the data show that the power spectral density of the simulated tunneling RTS is Lorentzian and that it follows the form predicted by theory as in Equation (3), verifying that the simulation code is producing reasonable results for the case of spin-*independent* tunneling events.

On and Off Resonance Results

Figure 6 shows the results of a simulation, driven both on and off magnetic resonance. The graphs on the left show the tunneling RTS signal (charge - top left), and the relative spin orientation (bottom left) for the off resonance case, while the graphs on the right show the same plots for the on resonance case. Regions where the electrons are

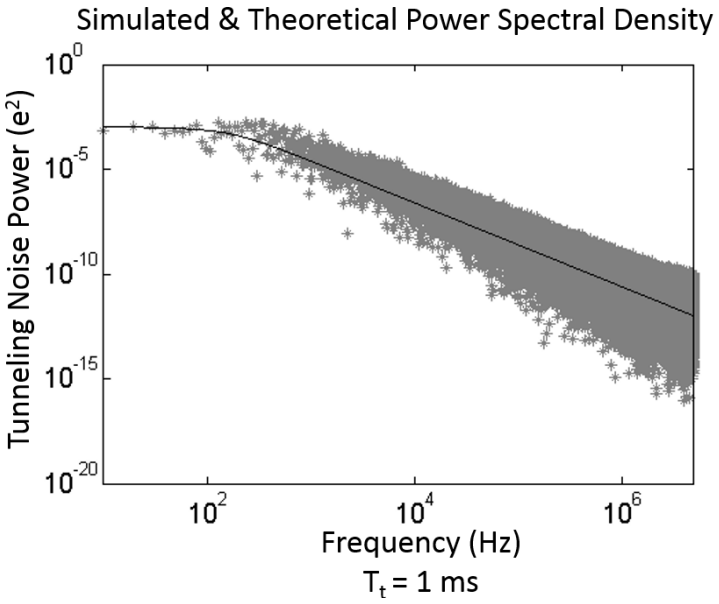

Figure 5: Lorentzian Power Spectrum. Black line is the theoretical power spectrum. The grey data points come from the simulated tunneling RTS power spectrum.

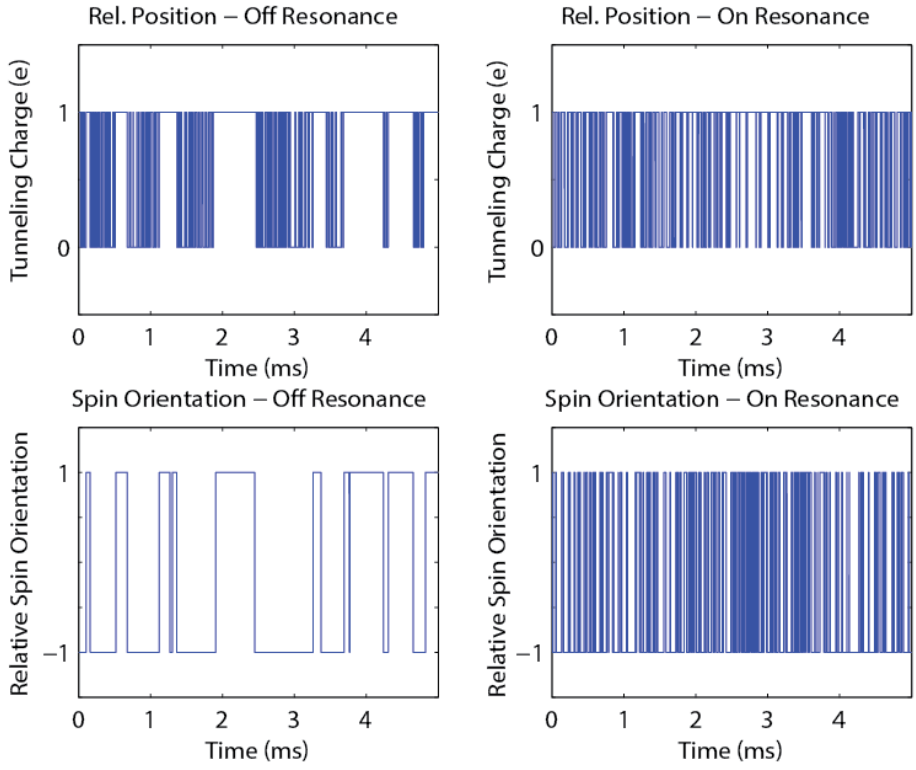

Figure 6: Tunneling RTS signal on (right) and off (left) magnetic resonance. The top row graphs represent the relative charge location. The bottom graphs are the relative spin orientation.

antiparallel and tunneling at a fast rate appear as a solid block.

The off resonance tunneling RTS signal shows many tunneling events when the electrons are separated and antiparallel and no tunneling events when the relative spin orientation is parallel. In contrast, the on resonance case shows many more *spin flip* events, because the spin is being magnetically flipped at a high frequency. This therefore allows many tunneling events to occur without the blinking effect. This occurs due to the shortened effective T_1 time which is smaller than the tunneling time for the on resonance case, when the applied rf field is large.

Average Charge

Because the AFM is capable of sensitive charge measurements, it is important to look at the average charge on the tip and on the sample in the on and off resonance case. If there is a change in the average surface charge between the system being driven on and off magnetic resonance, then the average surface charge (manifested in the cantilever frequency shift) could be used as the observable for detecting the single-spin signature.

For this example, the electron on the tip side will do the tunneling while the electron on the sample side will be stationary and can be considered charge neutral. For the off resonance case, with $T_1 > T_t$, many tunneling events occur back and forth while the spins are separated and antiparallel before a spin flip occurs. Thus, during this time of tunneling back and forth, the average charge on the tip is e/2. This charge (e/2) exists at the tip for an average duration of $2*T_1$, because for half of this time the electrons are together and cannot flip relative to one another. This is the first term in Equation (4). When the electrons are separated and spin blocked, the net charge on the tip is 1e. The average duration of this time period is T_1 (until a spin flip occurs). The sum of the two time periods

is 3*T_1. The average charge at the tip for the off resonance case is thus $\frac{2}{3}$ e (average charge at the sample is $\frac{1}{3}$ e), as shown in Equation (4).

$$\frac{\left(\frac{q}{2}\right)(2T_1) + (q)(T_1)}{3T_1} = \frac{2q}{3} \quad (4)$$

For the on resonance case, the effective spin lattice relaxation time is less than the average tunneling time T_t, and multiple spin flip events can occur while the electrons are separated. During this time a full charge 1e is found at the tip. The average duration of this time period is $2T_t$ because as the spin rotates fast, half the time it is spin blocked and unable to tunnel. This is represented by the first term in Equation (5). The second term represents the time when the electrons are together in the sample and therefore the charge at the tip is 0q. On average it takes a duration of T_t until an electron tunnels back to the tip state. Again the denominator represents the sum of the two time periods. For the on resonance case, the charge on the tip is also $\frac{2}{3}$ e ($\frac{1}{3}$ e on the sample).

$$\frac{(1q)(2T_t) + (0q)(1T_t)}{3T_t} = \frac{2q}{3} \quad (5)$$

The tunneling RTS simulations in Figure 7 verify that the average charge for both on and off resonance is the same, with an average of two-thirds of an electron charge at the tip (one-third charge at the surface), which agrees with the theoretical prediction. Because the average charge on and off resonance is the same, it is not possible to detect the magnetic resonance condition by measuring the average charge at the surface.

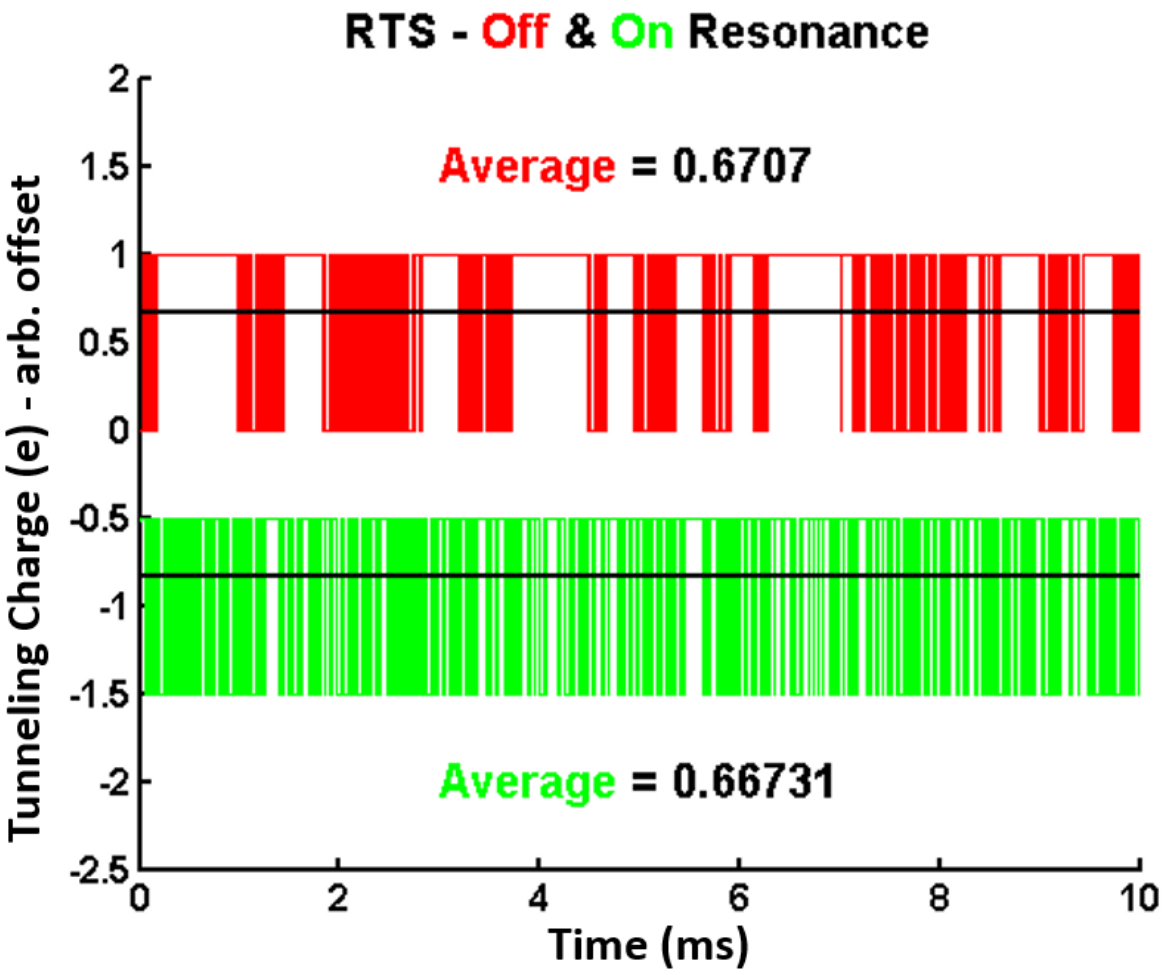

Figure 7: Tunneling RTS signal on and off magnetic resonance. Simulation correctly predicts and agrees with theory that the average charge at the tip is 2/3 for both on and off resonance cases.

Tunneling Charge Power Spectral Density

Even though the average charge is the same for both cases, the Power Spectral Density (PSD) of the tunneling RTS is different in the low frequency regime for the on and off magnetic resonance cases. Figure 8 shows the power spectral density in blue for the off resonance case and red for the on resonance case.

The higher spectral density in the low frequency range in the off resonance case results from the blinking that occurs, due to the times when the relative spins are parallel,

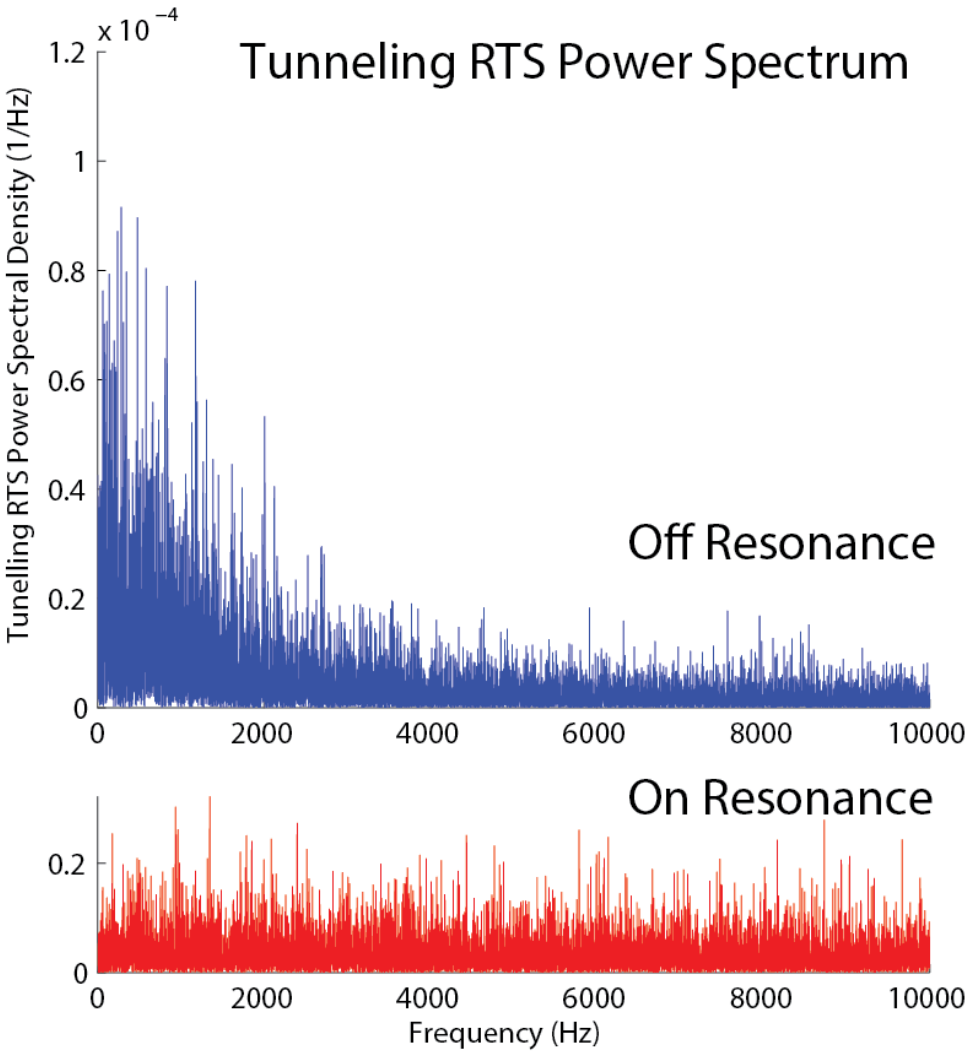

Figure 8: Tunneling RTS power spectral density. The difference in the tunneling RTS power spectral density at low frequencies between the system driven off (blue) and on (red) magnetic resonance can be used to identify the single electron spin signature.

which lasts for a relatively long time ($2T_1$). This low frequency component is absent in the on resonance case because the electron spin is being magnetically driven at the much higher rate. The two plots show that the tunneling RTS power spectral density is observably different and, therefore, it can be used to detect the magnetic resonance of an electron spin.

Detection Bandwidth

Any experimental implementation of this concept will be subject to a finite amount of detection bandwidth as shown in Figure 9. Each column shows, from left to right, the unfiltered time domain signal, filtered time domain signal, unfiltered power spectrum, and filtered power spectrum. A 1 kHz low-pass filter was used to simulate the measurement detection bandwidth. All simulations were performed with the same tunneling time of 10 μs. The tunneling only RTS ($T_1 >> T_t$) along the top row shows an average charge of one-half since there is an absence of spin blockade. There is, however, a noticeable difference between the root mean square (RMS) value of the time dependent, random telegraph signal, driven on and off magnetic resonance. This RMS value of the time dependent RTS is quantitatively related to the power spectral density of the tunneling charge noise and can be calculated within a given detection bandwidth.

The RMS of the tunneling noise driven off magnetic resonance is larger than the RMS of the tunneling noise driven on magnetic resonance for the filtered data (column 2), due to the longer spin blocked regions. These longer spin blocked periods are absent in the tunneling RTS driven on magnetic resonance, because the external driving magnetic field (B_1) causes the spin to flip more rapidly than the tunneling time.

All the filtered power spectra in column 4 show the data rolling off at 1 kHz. The power spectra show a clear difference between the tunneling RTS, on and off resonance cases. The off resonance power spectrum has a large low-frequency component whereas this component is much smaller in the on resonance case. Again, this is due to the fact that off resonance, there are longer periods of spin blockade ($2T_1$) due to the Pauli exclusion, which inhibits tunneling events and results in a larger low-frequency component in its power spectrum.

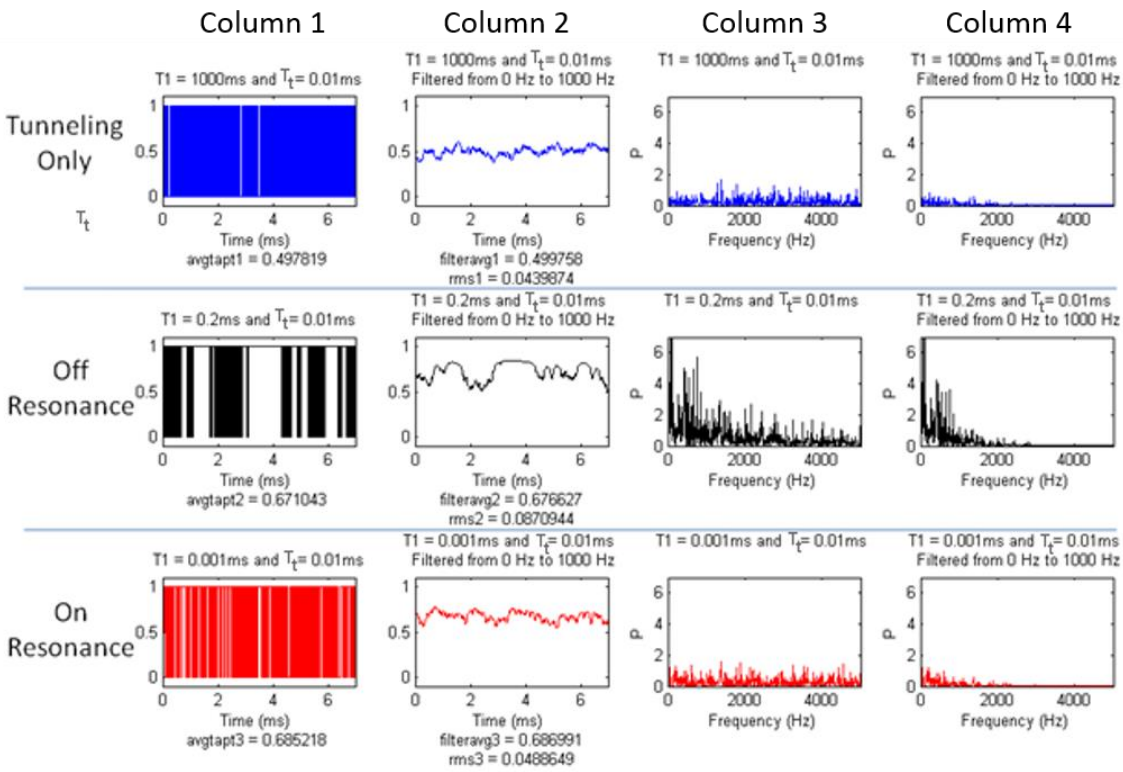

Figure 9: Tunneling RTS simulation summary Effects of Tunneling only, Off-Magnetic Resonance, and On-Magnetic Resonance respectively. For each row, the columns from left to right represent RTS-unfiltered, RTS-filtered (1 kHz), Power spectrum-unfiltered, Power spectrum-filtered.

Figure 10 shows the RMS of the tunneling noise signal as a function of the detection bandwidth applied. The red data set represents the off resonance case for T_1 = 200 µs and the green data set represents the on resonance case with an average spin flip time T_f of 1 µs. For both the on and off resonance curves, T_t = 10 µs. Between 10 and 1000 Hz, there is an appreciable difference between the RMS of the tunneling noise, on and off magnetic resonance. At high and low detection bandwidths, the difference between the RMS of the tunneling noise, on and off resonance goes to zero.

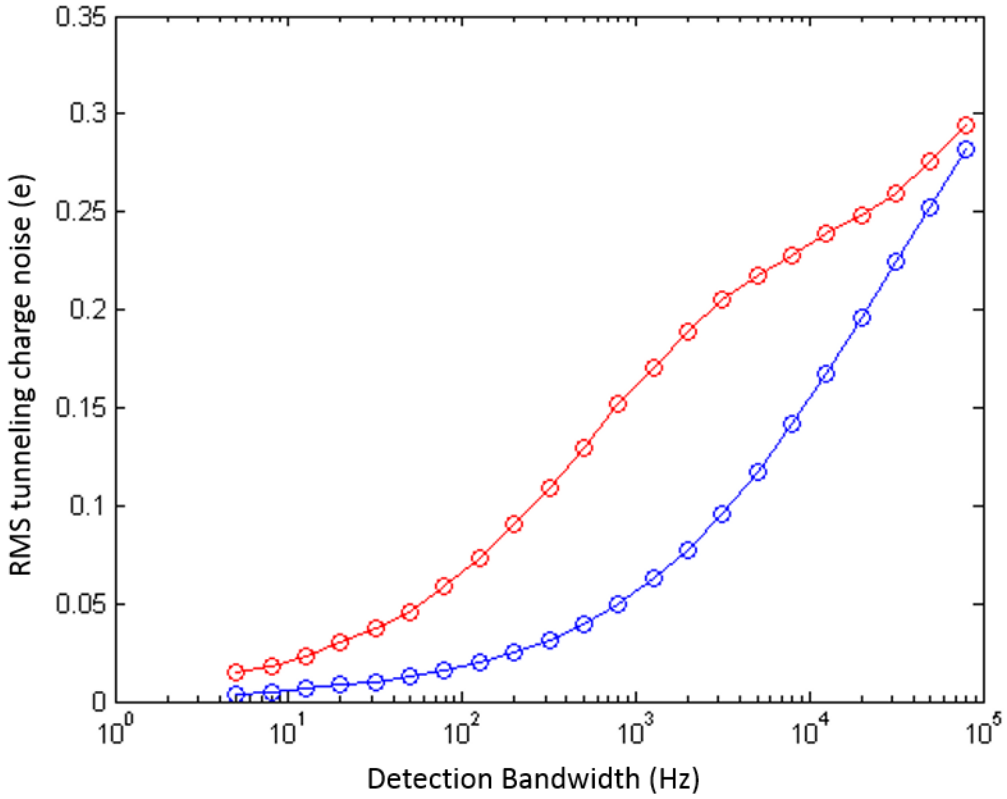

Figure 10: RMS of the tunneling noise on and off magnetic resonance vs. detection bandwidth. RMS of the tunneling noise for the system driven off (red) resonance and on (green) resonance vs. detection bandwidth for a tunneling time of 10 µs, T_1 = 200 µs, and T_f = 1 µs. This graph shows that there is a finite bandwidth region where the magnetic resonance signal is detectable with a maximum detectability in the middle.

Magnetic Resonance vs. Tunneling Time

Figure 11 shows the RMS of the tunneling noise for both the on resonance (red) and the off resonance (blue) cases, as the tunneling time is decreased from T_t = 25 s to T_t = 1 µs. The simulations run for 0.1 seconds. Experimental results have shown that the tunneling rate increases by an order of magnitude per Angstrom reduction of the tunneling gap.[1] Therefore Figure 11 effectively simulates the tip approaching the sample. For each data point, a tunneling RTS is simulated and the RMS of the tunneling noise is calculated and plotted vs. its tunneling time.

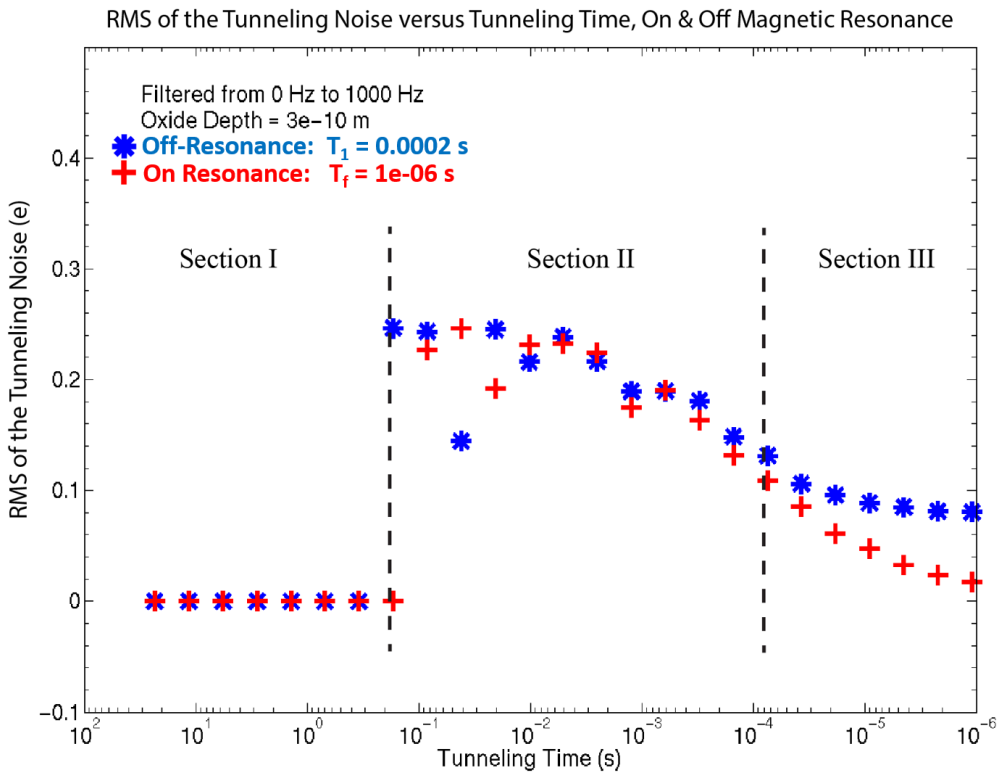

Figure 11: Tunneling noise vs. tunneling time Difference in RMS amplitude for on and off resonance as the tunneling time varies. This data shows that the single-spin signature is detectable when the tunneling rate is much faster than the spin lattice relaxation rate of $1/T_1$

In Section I, when the tunneling time is large, the RMS of the tunneling noise for both the on and off magnetic resonance cases are essentially zero because no tunneling events occur within the length of the simulation time (0.1 seconds). In Section II, starting around $T_t = 0.1$ s, tunneling events begin to occur at low frequencies and the RMS of the tunneling noise is at a maximum, because the low frequency components of the RTS signal easily pass through the filter. There is no difference between the RMS of the tunnel noise on and off magnetic resonance because the tunneling time, in this regime, is long compared to both T_1 and T_f and therefore achieving resonance does not significantly alter the RTS dynamics. In Section III, the difference between the RMS of the tunneling noise off and

on resonance becomes visible as the tunneling rate increases and $T_t << T_1$ (200 μs).

Under this condition, the off resonance signal has longer time regions of spin blockades, and, therefore, more low frequency noise. The on resonance signal has very short spin blockade time regions. Under this condition, RTS noise is more uniformly distributed, so that the noise within the detection bandwidth is lower. Figure 11 shows that in order to detect a magnetic resonance signature, the tip/sample gap must be small enough to achieve a tunneling rate that is much faster than $1/T_1$.

In conclusion, the simulation correctly predicts the dynamics of a tunneling RTS. The simulation results confirm that the average surface charge cannot be used as an observable for magnetic resonance. The simulation does, however, identify the RMS of the tunneling noise as a suitable observable for single-spin magnetic resonance. The simulation also establishes that the tip sample gap must be small enough to achieve a tunneling rate that is faster than $1/T_1$.

References

1. N. Zheng, C. C. Williams, E. G. Mishchenko, and E. Bussmann, J. Appl. Phys. **101**, 093702 (2007).

2. Y. Yamamoto, *Fundamentals of Noise Processes*. (Cambridge University Press, Cambridge, United Kingdom, 2002).

CHAPTER 3

AFM RESPONSE TO MAGNETIC RESONANCE

Choosing a Paramagnetic System

E' Center in Amorphous SiO_2

The E' center is a common defect found in SiO_2.[1-3] It is a silicon dangling bond created by an oxygen vacancy in amorphous[4, 5] SiO_2. It has many properties that make it an ideal candidate for the proposed single-spin measurement: the E' center is highly localized (less than 4 Angstroms[6]), which should allow its spin to be imaged with atomic scale resolution, it is electrically isolated from its environment since SiO_2 is a good dielectric, and the E' center is easily fabricated onto standard silicon AFM tips through thermal oxidation. Lastly, the E' center also has a relatively long T_1 (average spin lattice relaxation time) of 200 μs at room temperature.[7, 8] The simulation to this point has used this value of T_1 aiming to establish a way by which a single spin can be measured at room temperature.

There are many variations of E' centers found in amorphous SiO_2 due to the range of different bond angles and bond lengths found in the amorphous network. The common feature amongst all these variations is an unpaired electron on a silicon atom back-bonded to three oxygen atoms. Feigl et al.[4] identified an E' center in crystalline SiO_2 (initially called E_1') as a trapped hole on an oxygen vacancy. The unpaired electron is localized on the three fold coordinated silicon atom while a hole is trapped on the other silicon atom.

Amorphous SiO_2 has an analogous E' center known as the E'$_\gamma$ center, which also has a trapped hole on one of the silicon atoms and an unpaired electron on the other silicon atom. Rudra and Fowler[9] showed that the hole trapping silicon atom reaches a stable configuration by puckering behind the plane of the three oxygen atoms and bonding to a fourth oxygen atom in the amorphous network. The E'$_\gamma$ has an asymmetrical g tensor value of g_{11} =2.0018, g_{22} = 2.0006, g_{33} = 2.0003.

Griscom and Friebele[10, 11] found another E' variant, known as the E'$_\delta$ which has a symmetrical g tensor value of g_{11}=2.0018, g_{22}=g_{33}=2.0021. This suggests that the unpaired electron is shared between two silicon atoms. Chavez et al.[12] showed theoretical calculations that the unpaired electron is delocalized over the two silicon atoms and that this would produce a symmetric g tensor.

Nicklaw et al.[6] used density functional theory to simulate the different variations of E' centers found in amorphous SiO_2. Simulated defect free, a-SiO_2 structures were constructed with oxygen vacancies randomly distributed in the network. These oxygen vacancies immediately relaxed into Si–Si dimer configurations. These neutral dimer configurations were examined in both the positive and negative charge state, either by adding or subtracting an electron. The energies of these different arrangements, along with their energy width within the SiO_2 bandgap[13, 14] have also been calculated and tabulated.

Understanding the E' center system, and its paramagnetic properties, helps to identify important parameters (i.e., T_1 and the coulomb energy) needed to simulate the single-spin measurement and to determine its feasibility as a single-spin measurement system.

E' Center Energy Levels

In order for a localized paramagnetic electron in the tip to elastically tunnel to another localized electron in the sample, an energy condition must be met. Namely, the electron that tunnels over must have the same energy as the state which has the two electrons together after the tunneling event. When one electron tunnels over to the doubly occupied state, the coulomb repulsion generally raises the energy of the combined state. The coulomb energy between the singly occupied state and the doubly occupied state of the E'_{γ} center is approximately ~1eV.[15] With this energy condition met, the electron can elastically tunnel back and forth between singlet and product state with a tunneling rate that is governed by the tunneling barrier height and width.

Figure 12 represents the coulomb energy requirement for the two paramagnetic states to elastically tunnel between a doubly occupied singlet state and a separated product state. The horizontal axis is the spatial dimension while the vertical axis represents the energy of the states within the dielectric bandgap. The solid/dashed horizontal lines represent the energetic location of the singly/doubly occupied states, while the Gaussian curves represent the spread in energy of the singly/doubly occupied states. Notice the singly occupied state on the left (solid line) is energetically aligned with the doubly occupied state on the right (dashed line). If the Gaussian spread of the singly occupied state is comparable to the coulomb energy, there will be some states where an electron could randomly tunnel back and forth between the tip and sample. In the case that the Gaussian spread is much smaller than the coulomb energy, an external voltage bias may be necessary to align the states.

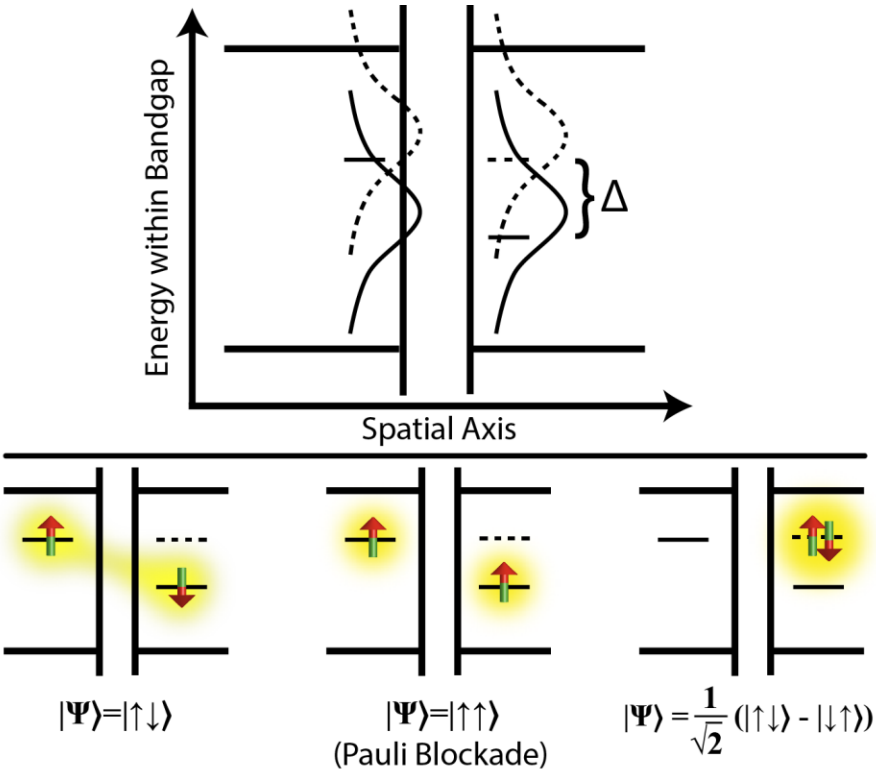

Figure 12: Energy diagram of the paramagnetic states meeting the coulomb energy requirement. (Top) The horizontal solid/dashed lines represent the energetic location of the singly/doubly occupied states. The solid/dashed line Gaussian curves represent the energy spread of the singly/doubly occupied states in the dielectric band gap. (Bottom) Energy diagram of the three possible charge and spin configurations of the probe-spin/test-spin pair.

Converting the Charge Noise to Cantilever Frequency Shift

Theoretical Model

In order to determine whether the theoretically predicted change in RMS tunneling noise due to spin resonance is detectable, a comparison with the detection sensitivity of an actual AFM system is required. To accomplish this, a theoretical model, diagramed in Figure 13, is used to calculate the change in frequency shift of an oscillating AFM cantilever caused by a single electron tunneling event between the tip and sample states. This calculation is used to properly scale the simulation results (with output 0 or 1) to an

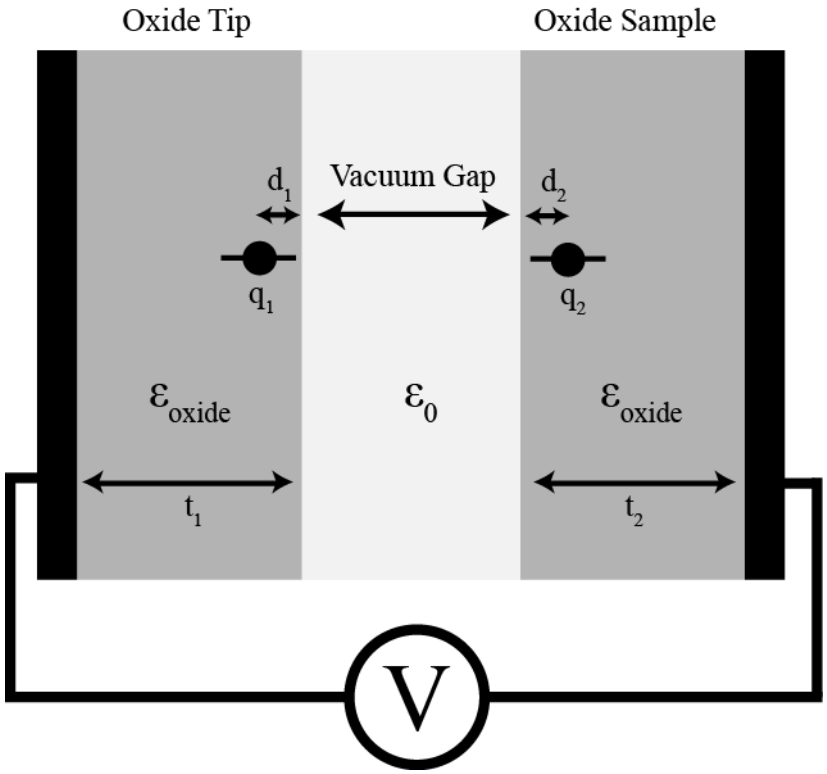

Figure 13: 1D Electrostatic model of the tip/sample and defect states under an applied voltage bias. The electrostatic force gradient is calculated for two cases: 1) one electron in each defect state (separated charges), 2) electrons are together in the doubly occupied defect state in the sample (charges together). The difference in force gradient is converted into a difference in frequency shift. This difference in frequency shift is used to scale the simulation results.

actual frequency shift of the AFM cantilever for a given set of experimental parameters. The first step toward determining this "scaling factor" is to calculate the change in the electrostatic force gradient on the tip produced by an electron tunneling from a defect state in the tip oxide to a defect state in the surface of the sample oxide. In this one dimensional calculation, it is assumed that the depth of both states is small (0.2 nm), which is small compared to the oxide thicknesses (tip oxide: 10 nm and sample oxide: 15 nm). The two defect states are schematically shown in Figure 13 with the relevant electrostatic parameters.

The one dimensional electrostatic force gradient is calculated for the two occupancy

cases: 1 charge in each defect state (separated) and both charges in one state (together) as a function of several parameters including vacuum gap, oxide thickness, depth of each state, and external voltage bias. This calculation includes the effects of the polarization of the oxide. This Coulombic force gradient is then converted into an AFM cantilever frequency shift[16] using experimental AFM parameters (spring constant, resonance frequency, oscillation amplitude and an applied voltage of 10 volts). Using these values, the magnitude of the frequency shift caused by a single electron tunneling event (scaling factor) is calculated to be between 11.4 Hz and 13.0 Hz for tip-sample oxide vacuum gaps ranging between approximately 6.0 Angstroms to 0.5 Angstroms. This scaling factor (at different tip-sample gaps) is used to scale the simulated tunneling charge noise to AFM frequency shift noise. Previous work by Jon Johnson calculated the force gradient between two point charges, each in its own dielectric material, separated by a vacuum gap and without an applied external voltage.[17]

Since two randomly chosen states in the sample and tip oxides may not have the appropriate energies for elastic tunneling between them, i.e., the energy of the singly occupied tip state may not be equal to the energy of the doubly occupied sample state (or vice versa), an external voltage bias may be necessary to bring these two states into energy alignment. With 10 volts applied across the oxide films and tip-sample gap, only part of this voltage is dropped between the two states, shifting their relative energies. A relative energy shift of 1 eV is accomplished with a 6 Angstrom vacuum gap and a 10 volt applied bias. Under these conditions, the applied electric field is approximately 4-5 MV/cm which is less than the breakdown field of silicon dioxide (~10 MV/cm).[18]

Dependence of Magnetic Resonance Signal on RF Frequency

The location of the magnetic resonance dip (rf frequency) depends on the strength of the static magnetic field B_0 according to the relationship in Equation (6)

$$\boldsymbol{B_0 = h\nu / g_e \mu_B} \quad (6)$$

where B_0 is the static magnetic field strength, h is Planck's constant, ν is the rf magnetic field frequency, g_e is the Landé g-factor, and μ_B is the Bohr magneton. Assuming the static magnetic field is well known, sweeping the rf magnetic field and identifying the magnetic resonance frequency enables the measurement of a unique Landé g-factor for that particular paramagnetic defect. The Landé g-factor is related to the quantum mechanical spin and angular momentum of the particular state that the electron occupies.[19] The g-factor for a free electron is $g_e = 2.0023$.[20] A measured g-factor, when combined with other compositional constraints, could potentially be used to determine the chemical identity of a particular paramagnetic defect by comparing the measured value with previously published g-factor values for known defects.

The simulation has predicted the tunneling RTS spectrum for the two electron system driven exactly on and off resonance. By using Rabi's formula and Fermi's Golden rule[21] and assuming a g-factor equal to 2, one can calculate the spin flip rate as a function of the applied B_1 frequency. The spin flip rates are then used in the simulation in generating random spin flip times as outlined in the computational algorithm. This allows, as shown in Figure 14, the simulation of the RMS of the tunneling noise as a function of the rf field frequency as it is swept through magnetic resonance. In Figure 14, each simulation time series is repeated 10 times and the standard deviation in the RMS of the tunneling charge noise is represented through the error bars.

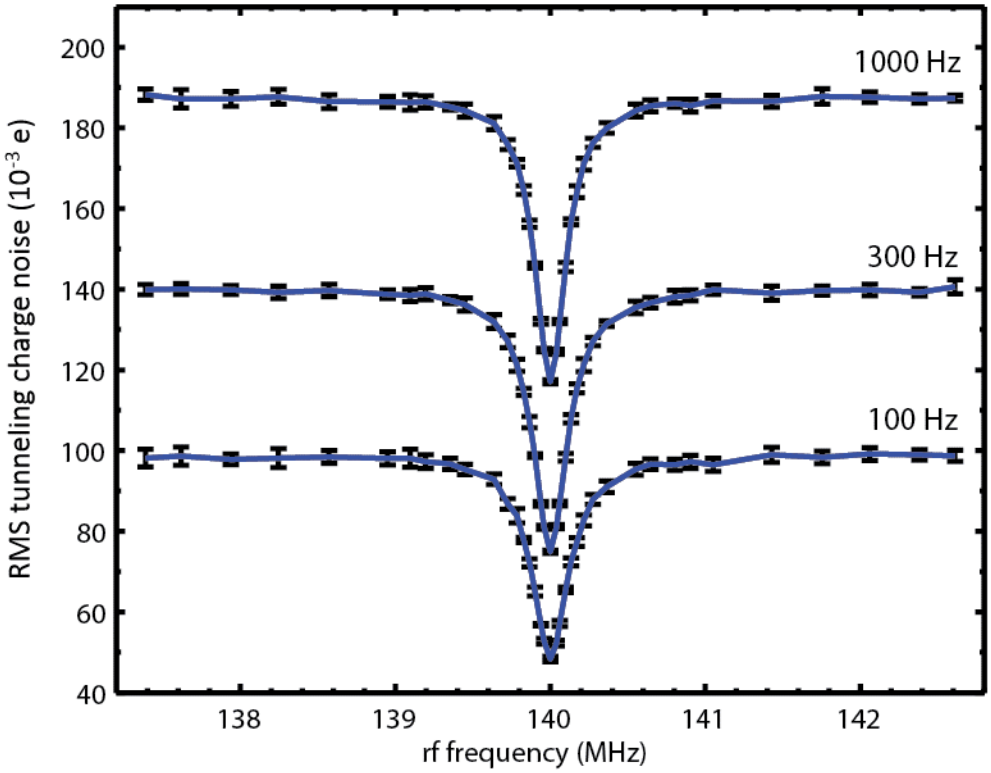

Figure 14: RMS of the tunneling noise vs. rf frequency for various detection bandwidths. Each error bar represents the standard deviation of ten, 1 second simulations. For each simulation, filtering is applied, and the root mean square value of the tunneling RTS is calculated. The different curves were taken at different detection bandwidths as labelled above each curve. Each curve was taken with T_1 = 200 us, tunneling time T_t = 10 us, B_1 amplitude of 50 mGauss, and a simulation time of 1 second.

As the detection bandwidth decreases, the baseline decreases as more of the tunneling noise is being filtered out. The difference between the on and off resonance signal also decreases with decreasing detection bandwidth, because the total integrated power spectrum (RMS), within the detection bandwidth, becomes smaller for both the on and off resonance cases.

In Figure 15, the RMS of the tunneling charge noise is plotted as a function of rf frequency at rf magnetic field strengths (B_1) varying from 0.1 μT to 100 μT, for a static

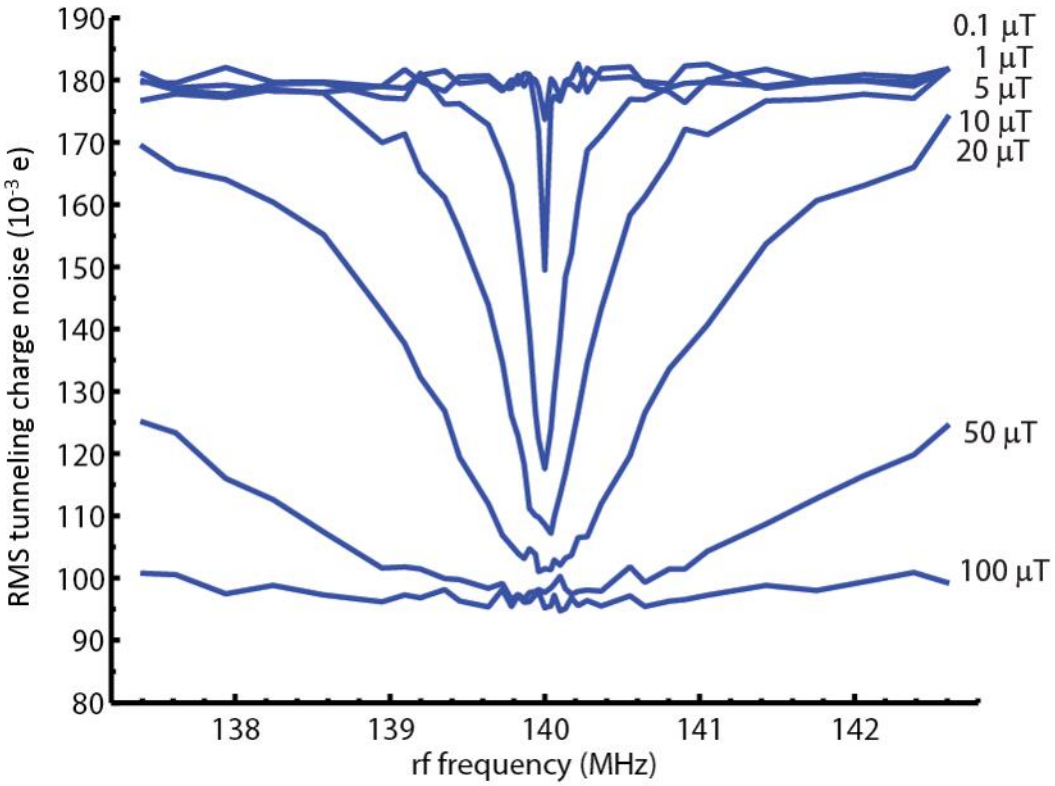

Figure 15: RMS of the tunneling noise vs. rf frequency for various B_1 strengths. Each data point represents a single 1 second simulation. Error bars have been omitted for clarity. For each time trace, the bandwidth is applied, and the RMS of the tunneling noise is calculated. The different curves were taken at different B_1 strengths as referenced on the right hand side. Each curve was taken with T_1 = 200 us, tunneling time T_t = 10 us, and a detection bandwidth of 1000 Hz.

magnetic field (B_0) of 5 mT. Each data point represents a single 1 second simulation. The error bars have been omitted for clarity. At low B_1 amplitudes, the resonance dip is indistinguishable from the off resonance tunneling noise. As the B_1 amplitude increases, the magnetic resonance signature increases in visibility. The faster on resonance flip rate produces a smaller tunneling noise after filtering and, therefore, the magnetic resonance dip deepens. The resonance signal is also power broadened according to Rabi's formula[21] as the B_1 amplitude increases. The power broadening increases the width of the resonance dip and therefore makes it easier to find.

There are some obvious advantages to using high power rf magnetic field amplitudes. Broadening the dip will make it easier to identify the resonance when sweeping the B_1 frequency for the first time (especially if the uncertainty in B_0 is large). Also, increasing the resonance depth of the dip also makes it easier to find. However, there are some practical limitations. Increasing the rf coil power will also increase the temperature of the system and therefore increase the thermal drift of the system. This is especially problematic for identifying the single-spin detection for the first time if it takes a long time to sweep the rf magnetic field.

Scaled AFM Magnetic Resonance Response

Figure 16 shows the simulated on and off resonance frequency shift noise as a function of detection bandwidth and rf frequency, after proper scaling using the scaling factor calculated in Chapter 3.

The red and blue curves in the left panel of Figure 16 show the RMS of the tunneling noise, off and on magnetic resonance for various tip sample gaps ranging from approximately 0.5-6.0 Angstroms. The table shows the energy shift Δ (eV) of the probe and test state produced by an applied voltage of 10 volts at the different tip-sample gaps. The curves in the right panel of Figure 16 represent the simulated RMS of the tunneling noise as a function of rf frequency for various levels of detection bandwidth. The error bars on the blue resonance curves represent the standard deviation of the RMS of the tunneling noise obtained from many simulations, each with a total simulation time of 1 second per frequency step.

The size of the standard deviation depends on how the bandwidth and simulation

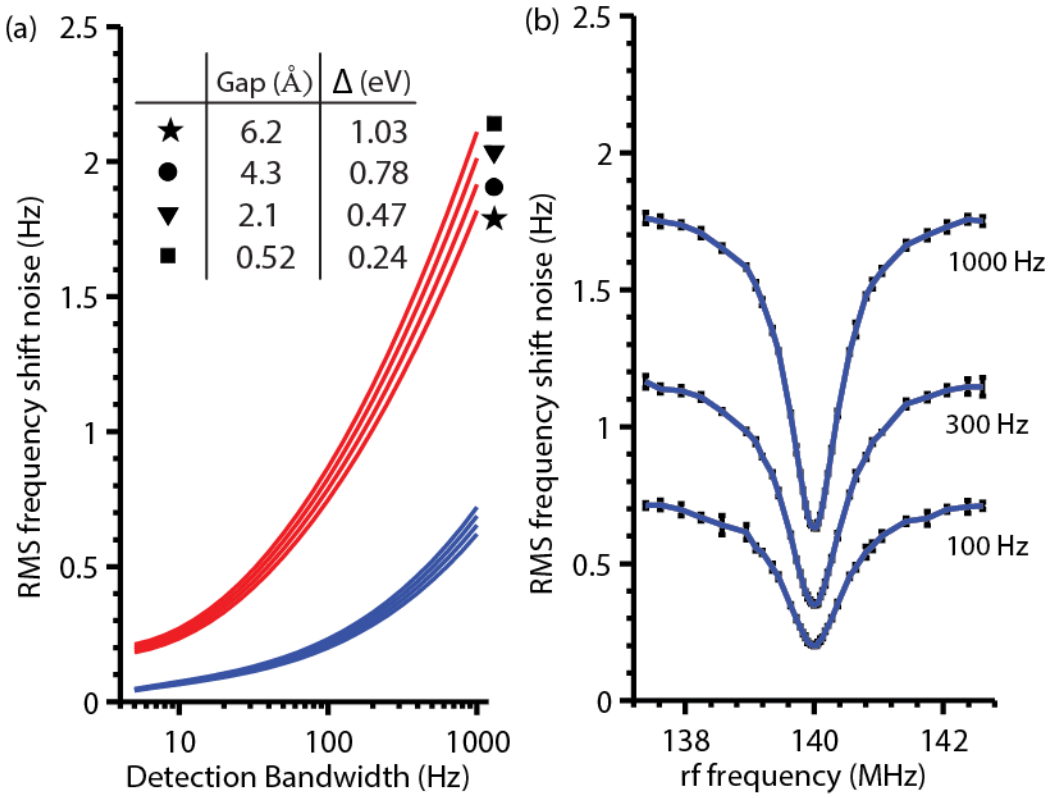

Figure 16: Converting the simulation into an AFM frequency shift and magnetic resonance dip. The left panel shows the RMS of the tunneling noise for the off (red) and on (blue) magnetic resonance conditions as a function of detection bandwidth. The black symbols connect the red and blue pairs with their respective gaps and the energy shift achieved when a 10 volt bias is applied. The right panel shows the resonance dip in the RMS of the frequency shift noise, due to spin dependent tunneling, as the rf frequency is swept for various levels of detection bandwidth. The standard deviation of the amplitude is shown in the error bars. These results do not take into account system noise.

time (experimentally this is the dwell time per rf frequency step) are chosen, with considerations to the physical processes involved (T_1 and T_t). In order to detect the magnetic resonance dip, the standard deviation of the RMS of the tunneling noise ("noise" on the resonance dip) should be smaller than the signal size (difference between the off and on resonance RMS values).

The graphs in Figure 17 show that the signal to noise decreases as the total simulation time is decreased from 100 ms in graph (a) to 1 ms in graph (c). Shorter

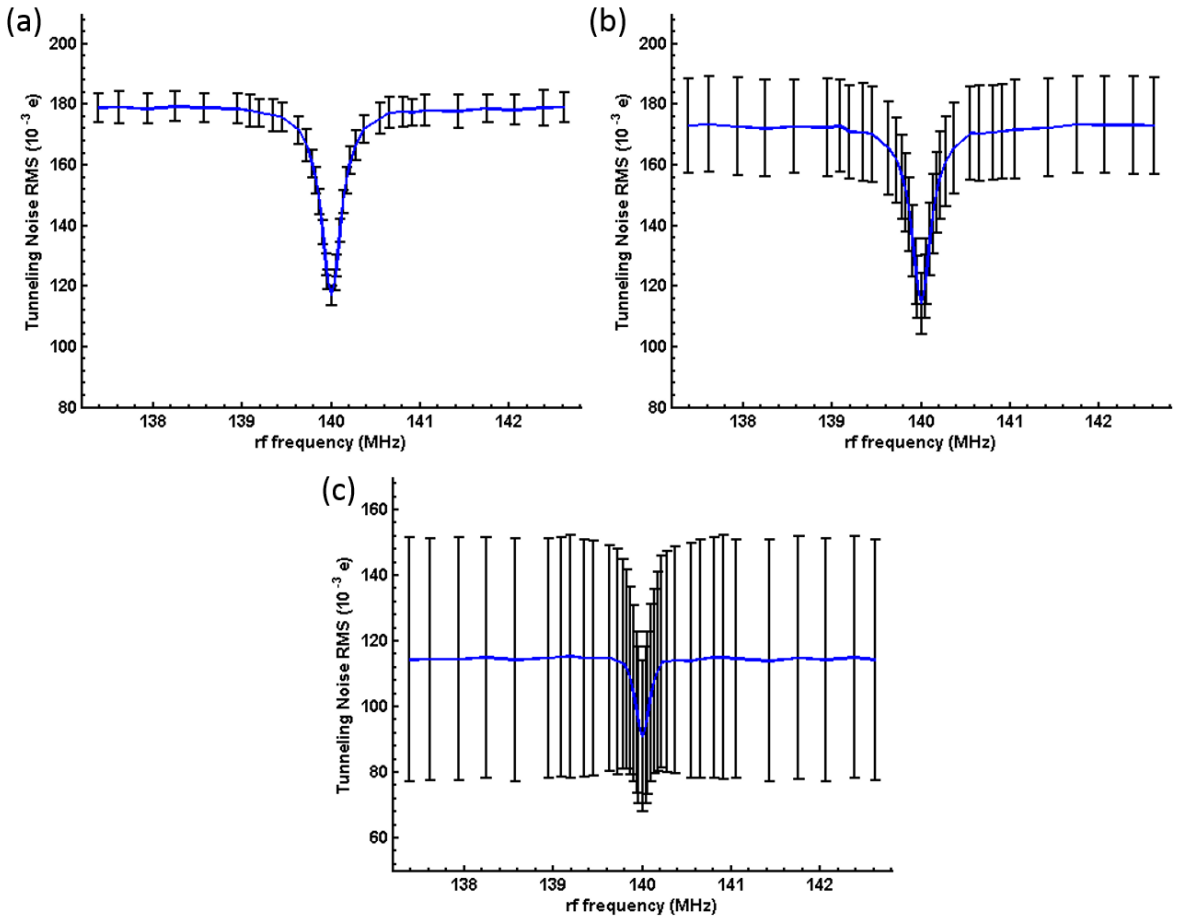

Figure 17: S/N ratio vs. the total simulation time. The three graphs (a), (b), and (c) show the resonance dip in the RMS of the tunneling noise as the rf frequency is swept for varying simulation times. Experimentally, the total simulation time is equivalent to the dwell time per rf frequency step. The graphs show that the signal to noise ratio decreases as the total simulation time decreases from 100 ms in graph (a) to 10 ms in graph (b) and to 1 ms in graph (c).

simulation times record fewer tunneling events and, therefore, the standard deviation increases. This S/N ratio does not take into account the AFM system noise.

The next chapter will discuss the experimental optimizations to the system that reduced the overall AFM system noise level. It will also discuss how the system noise is measured in the presence of tip sample interactions. Finally, the measured system noise level will be compared with simulation results.

References

1. P. M. Lenahan and P. V. Dressendorfer, J. Appl. Phys. **55**, 3495 (1984).

2. P. M. Lenahan and J. F. Conley, IEEE Trans. Nucl. Sci. **45**, 2413 (1998).

3. D. M. Fleetwood, P. S. Winokur, R. A. Reber, T. L. Meisenheimer, J. R. Schwank, M. R. Shaneyfelt, and L. C. Riewe, J. Appl. Phys. **73**, 5058 (1993).

4. F. J. Feigl, W. B. Fowler, and K. L. Yip, Solid State Commun. **14**, 225 (1974).

5. S. P. Karna, A. C. Pineda, R. D. Pugh, W. M. Shedd, and T. R. Oldham, IEEE Trans. Nucl. Sci. **47**, 2316 (2000).

6. C. J. Nicklaw, Z. Y. Lu, D. M. Fleetwood, R. D. Schrimpf, and S. T. Pantelides, IEEE Trans. Nucl. Sci. **49**, 2667 (2002).

7. S. S. Eaton and G. R. Eaton, J. Magn. Reson., Ser A **102**, 354 (1993).

8. B. T. Ghim, S. S. Eaton, G. R. Eaton, R. W. Quine, G. A. Rinard, and S. Pfenninger, J. Magn. Reson., Ser A **115**, 230 (1995).

9. J. K. Rudra and W. B. Fowler, Phys. Rev. B **35**, 8223 (1987).

10. D. L. Griscom and E. J. Friebele, Phys. Rev. B. **34**, 7524 (1986).

11. R. A. Weeks, J. Non-Cryst. Solids **179**, 1 (1994).

12. J. R. Chavez, S. P. Karna, K. Vanheusden, C. P. Brothers, R. D. Pugh, B. K. Singaraju, W. L. Warren, and R. A. B. Devine, IEEE Trans. Nucl. Sci. **44**, 1799 (1997).

13. N. L. Anderson, R. P. Vedula, P. A. Schultz, R. M. Van Ginhoven, and A. Strachan, Phys. Rev. Lett. **106**, 206402 (2011).

14. N. L. Anderson, R. P. Vedula, P. A. Schultz, R. M. Van Ginhoven, and A. Strachan, Appl. Phys. Lett. **100**, 172908 (2012).

15. B. Tuttle, (Private Communication).

16. U. Durig, Appl. Phys. Lett. **75**, 433 (1999).

17. J. Johnson, Ph. D. thesis, University of Utah, 2010.

18. S. M. Sze, *Physics of Semiconductor Devices*. (Wiley-Interscience Publication, Murray Hill, New Jersey, 1981).

19. J. S. Townsend, *A Modern Approach to Quantum Mechanics*. (University Science Books, Sausalito, California, 2000).

20. B. Odom, D. Hanneke, B. D'Urso, and G. Gabrielse, Phys. Rev. Lett. **97**, 030801 (2006).

21. J. J. Sakurai, *Modern Quantum Mechanics.* (Addison-Wesley Publishing Company, Reading, Massachusetts, 1994).

CHAPTER 4

EXPERIMENTAL PREPARATIONS AND COMPARISONS OF SIMULATION RESULTS WITH NOISE MEASUREMENTS

AFM Preparation

A number of modifications to a commercial AFM (Omicron AFM/STM S) were made in preparation for the single-spin detection experiment. This section will describe the different components and modifications, specific to the single-spin experiment, including the rf coil installation and calibration, the data acquisition software, the generation of high density E' samples, and optimization of the optical beam deflection system. After all these improvements to the system, the system noise was carefully measured in the presence of tip sample interactions. These results are then compared to the theoretical simulation results to determine the detectability of the magnetic resonance signature of a single spin.

RF Coil Design, Calibration and Installation

In order to flip the spin of the telegraphing electron, an rf coil was designed, calibrated and installed into the UHV chamber. Simulations showed that a flip time induced by an rf magnetic field needs to be much shorter than the natural spin lattice relaxation time T_1 of the state to which the electron tunnels. Research performed by K. Ambal[1] showed that at high density ($10^{18}/cm^3$), E' defects have a T_1 time of ~200 us at room temperature. Therefore, a spin flip rate of 10 us is suitable to detect a difference in

the RMS of the tunneling noise on and off resonance.

The necessary rf field strength can be calculated from Equation (7) where B_1 is the rf magnetic field strength (perpendicular to the static magnetic field B_0), γ_g is the gyromagnetic ratio, and t_f is the average spin flip time. The factor of 2 is due to the fact that only a 180º spin flip is required.

$$\boldsymbol{B_1 = \frac{1}{2\gamma_g t_f}} \tag{7}$$

An average spin flip time of 10 us corresponds to an rf field strength of approximately 20 mGauss.

The rf coil was fabricated at the University of Utah (William's Lab) using kapton coated magnet wire (34 AWG). The coil was then attached to a coax cable and electrical feed-through UHV flange. The rf source, all coax cables and any necessary connectors were impedance matched to 50 Ω in order to minimize any power losses due to reflections. The total cable length from coil to rf source was 1.6 meters.

The rf magnetic field was measured as a function of rf frequency, using a magnetic field probe (calibrated coil) that was purchased from Beehive Electronics Inc. (model no. 100B EMC). The measured results were also compared to a theoretical simulation of the rf coil setup using parameters and specifications from the fabricated coil. The results are shown in Figure 18, where the blue points are the simulated data, the red points are the measured data and the green line is the 20 mGauss minimum field required to flip the spin by 180º in 10 μs.

Although there are regions where the measured magnetic field is less than the 20 mGauss threshold, the difference is always less than a factor of two. Since the measured T_1 time of the E' centers (~200 us) is much greater than the spin flip time (10 us) by a

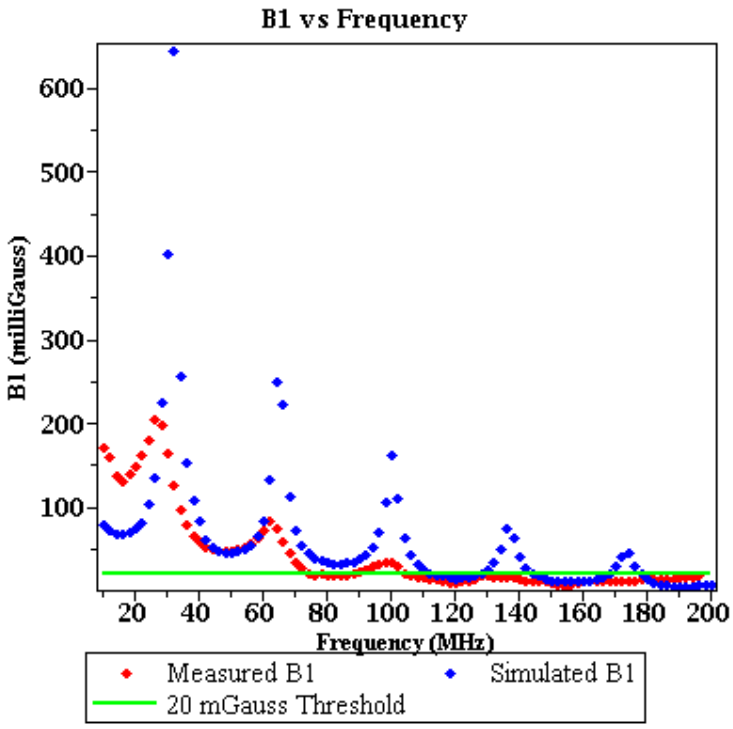

Figure 18: RF coil calibration. B_1 measurements (red points) of the fabricated coil are compared to theoretical calculations of the rf coil (blue points). The green line represents the minimum B_1 amplitude needed to flip an electron spin in 10 μs.

factor of 20, the slightly weaker measured B_1 field is still suitable to see a difference in the RMS of the tunneling noise on and off resonance. It should also be noted that the coil was measured outside the UHV chamber and part of the rf power was split off as a reference signal to a lock in amplifier (50 Ω input impedance), further reducing the rf field strength. The field strength during the actual experiment will be larger when the LIA is gone. Figure 19 shows the rf coil mounted on a modified sample holder. The setup allows samples to be interchanged easily between single electron spin measurements and regular AFM measurements. When the sample is in place, the rf coil is approximately 3 mm from the AFM tip.

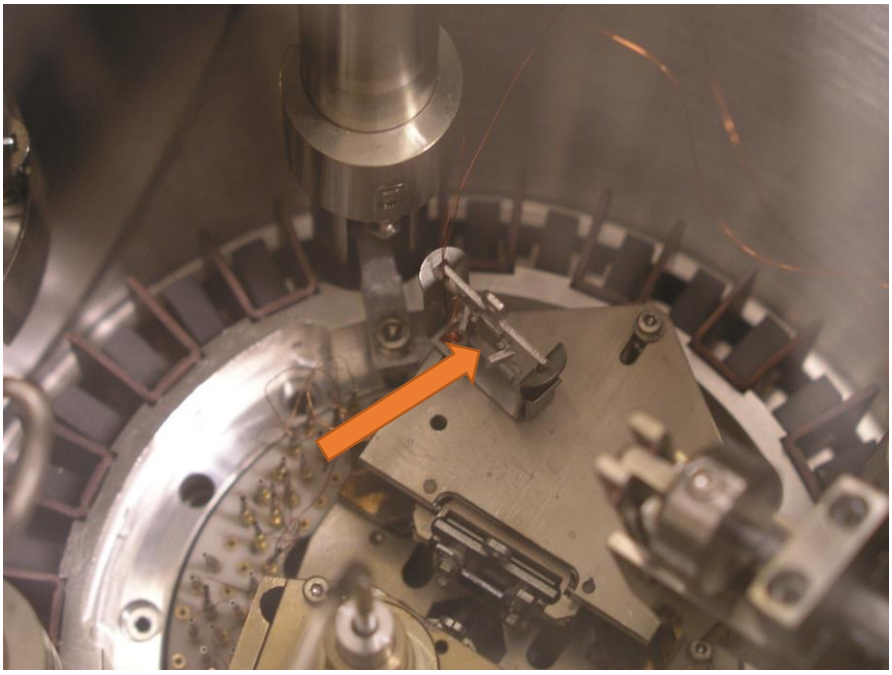

Figure 19: RF coil glued in place to a tip transfer plate that is moveable via a manipulator arm between the pictured location and the microscope sample position in the AFM UHV chamber. A sample is glued to a modified STM tip holder (not shown), which is then placed in the tip transfer plate for magnetic resonance experiments.

Software and Theoretical Analysis for Frequency Sweep and Noise Measurement Program

The methodology to detect a single electron spin requires control software that records the frequency shift noise from the AFM while sweeping the rf frequency sent to the rf coil. LabVIEW was used to write a frequency sweep program and to interface it with the AFM and rf coil setup.

Equation (8) calculates the magnetic resonance frequency for a given static

$$\boldsymbol{f = \gamma_g B_0} \tag{8}$$

magnetic field B_0 and determines the frequency sweep range that the LabVIEW program will use. For $B_0 = 50 \pm 5$ Gauss, the resonance frequency is expected to be 141 ± 14 MHz. As the rf (B_1) field is swept between 141 ± 14 MHz, the software collects frequency shift

data (df) at each rf frequency interval. The RMS of each frequency shift data is calculated and, finally, a graph of the frequency shift noise vs. the rf (B_1) frequency is produced. From this, we expect to see the magnetic resonance signature of the single electron. Also, in order to accurately resolve a resonance dip from the frequency shift signal, the rf frequency intervals must be sufficiently small compared to the expected linewidth of the resonance. In this experiment, the linewidth due to the applied rf magnetic field ($\sim 1/t_f$) is expected to be much greater than the intrinsic linewidth due to the electron's spin-lattice interaction ($\sim 1/T_1$). Therefore, the resonance linewidth should be on the order of $1/t_f$ and the rf frequency sweep time intervals should be small compared to that frequency. This allows the resonance dip to be resolved with multiple data points. The detection bandwidth of the AFM is only 1000 Hz. Therefore, the frequency sweep software collects data at a sampling rate of 10 kHz (oversampled). Finally, the sweep program needs to be fast enough so that the tip does not move away from the E' center due to thermal drift. These are some of the considerations put into the design of the frequency sweep program. The screen shot in Figure 20 shows the frequency sweep program in its current state.

E' Generation Methods

A thermal oxide sample with a high density of E' centers is needed in order to find a paramagnetic center and to perform the single-spin experiment, all within a reasonable amount of time. One can estimate the required density for a probe tip radius of 25 nm and a tunneling depth of 0.5 nm to be in the range of $10^{18} - 10^{19}$ spins/cm^3. As most of the research on E' centers is focused on techniques that reduce the density, various methods had to be explored that could potentially increase the density. The following methods were used to try to achieve those densities: (1) ultraviolet radiation[2] with a NdYAG laser (264

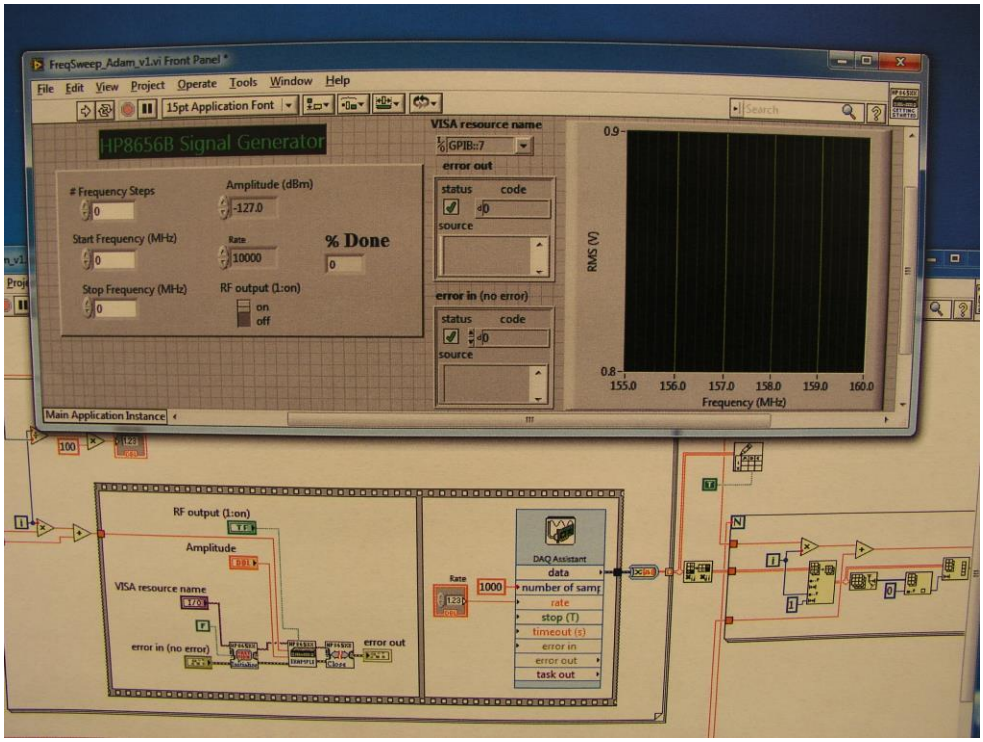

Figure 20: Frequency sweep program written in LabVIEW to acquire the frequency shift df for a set amount of time per rf frequency step. The root mean square of each df time trace is calculated in real time and plotted vs. its corresponding rf frequency.

nm wavelength), (2)gamma radiation[3] (Cs-137) for 24 hours (10-12 Mrad total dosage), and (3) different growth temperatures during the thermal oxidation process. These methods were unsuccessful in producing densities higher than the sensitivity of the CW-ESR instrumentation ($10^{17}/cm^3$). The most successful method used was an Ar-ion discharge plasma[4, 5] excited by a 300 W, 13.56 MHz RF excitation at 0.5 sccm gas flow and a pressure of 10 mTorr. Target E' densities were achieved and were characterized for their spin properties by K. Ambal.[1] These measurements showed that these E' centers had a T_1 of approximately 200 μs at room temperature and at high densities.

AFM Optimization

Replacing LED Light Source With an External Laser Diode Setup

As the AFM probe is raster scanned over a surface, the oscillating tip, at the end of a cantilever, interacts with the surface, as shown in Figure 21. These force interactions are sensed by monitoring the change in resonance frequency of the oscillating cantilever. This change in resonance frequency is monitored by a light beam which reflects off the end of the cantilever and is detected by a four quadrant silicon photodetector.

The factory installed LED light source was replaced with a laser diode setup. The laser diode allows the AFM beam deflection system to operate with an adjustable light source power. Theoretical calculations will show in the next section that the AFM signal to noise ratio improves with larger optical power from the light source.

The new light source is a pigtailed, single mode, 830 nm laser diode (Thorlabs LPS-830-FC), and is controlled using a laser diode/TEC controller (SRS LDC501). This wavelength was chosen to closely match the emission wavelength of the LED light source already in the AFM system. The fiber is fed into the vacuum system through a CF-flanged optical fiber feed-through (LewVac FO-SM800-40CF) which is UHV compatible down to 10^{-10} Torr. The in-vacuum fiber is also UHV compatible by means of a CuBALL metal coating (Oxford Electronics); the coating provides a hermetic seal and allows the fiber to keep its structural integrity with exposure to bake-out temperatures of 200 C. The end of the fiber was attached to a zirconia ferrule and then to a metal cylinder. The metal cylinder allows the laser diode to mount to the existing light source housing structure inside the AFM. The end of the fiber was cut and polished almost perpendicular to its axis.

Finally, the LD light source is fitted with an optical isolator and an optical attenuator outside the vacuum system. The isolator minimizes any back reflection coming

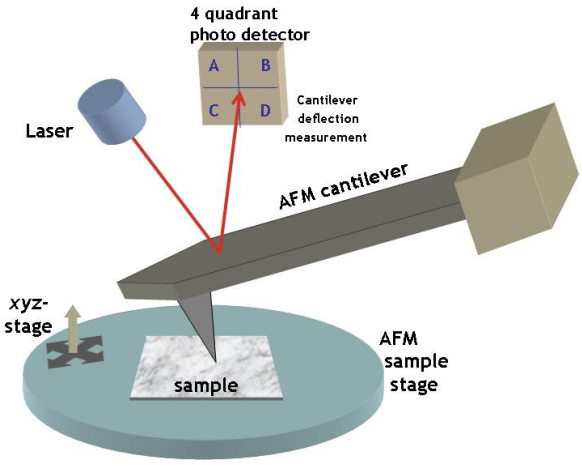

Figure 21: Typical optical beam deflection system in an AFM. Illustration made available by the Opensource Handbook of Nanoscience and Nanotechnology, (CC-BY-2.5)

from the ends of the UHV fiber (typical peak isolation of 25 dB) and the attenuator adjusts the power in order to avoid saturating the AFM photodetector.

Deflection Noise Spectral Density

The deflection signal FN is found by taking the difference in intensities between the top two quadrants and the bottom two quadrants. The deflection (amplitude) noise spectral density of the system D_{SD} (see Equation (9)) is given by multiplying the voltage noise density N_{SD} (the voltage noise on the FN signal) with the cantilever sensitivity S (deflection in meters/volt of signal output by the FN signal), shown in Equation (9).

$$\boldsymbol{D_{SD} = N_{SD} * S} \tag{9}$$

Increasing the light source power also increases the overall deflection (amplitude) noise spectral density on the photodetector by increasing the shot noise, according to Equations (9), (10) and (11)

$$\boldsymbol{N_{SD}^2 = N_{shot}^2 + N_{system}^2 G^2} \tag{10}$$

$$\boldsymbol{N_{shot}^2 = 2q\alpha P_D R^2 G^2} \tag{11}$$

where N_{shot} is the shot noise voltage spectral density, N_{system} is the electronic noise volume of the system on the FN signal, q is the electron charge, α is the photodetector responsivity, P_D is the power hitting the photodetector, R is the gain of the transimpedance amplifier, and G is the gain on the signal. The shot noise (N_{shot}) and system noise (N_{system}) are assumed to be uncorrelated noise sources and must be properly summed to get the total voltage noise spectral density (i.e., sum of squares).

With the modifications to the AFM light source, the voltage noise on the deflection signal (FN channel) was measured as a function of the optical power hitting the photodetector (P_D). Figure 22 shows the relationship between the noise power spectral density (N_{SD}^2) and the optical power (P_D).

Turbrugge et al.[6] showed that the sensitivity S (nm/V) is inversely proportional to the amount of light hitting the photodetector, Σ_{in} (voltage sum from all 4 quadrants of the photodetector), and therefore inversely proportional to the amount of power coming from the light source. This relationship is shown in Equation (12), where S is the sensitivity of the cantilever (nm/V), and β is a proportionality constant that relates the sensitivity of the cantilever (S) to the amount of power hitting the photodetector(P_D) and is unique to the individual characteristics of that particular probe.

$$\boldsymbol{S = \frac{\beta}{P_D}} \tag{12}$$

Figure 23 shows measurements taken at the University of Utah relating the sensitivity S to the optical power hitting the AFM detector after the modifications to the AFM light source. Calculating β from the slope of Figure 23 produces a value of β = 1.18e-12 Wm/V.

By combining Equations (9) through (12), the deflection noise spectral density can

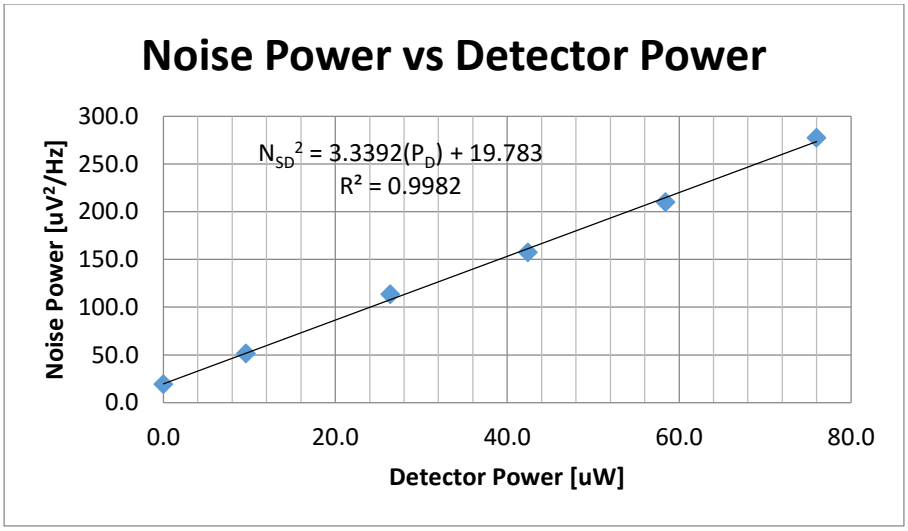

Figure 22: Noise power spectral density vs. detector power. The noise power spectral density on the deflection signal (FN) was measured as a function of optical power hitting the four quadrant photodetector. The increased optical power increases the shot noise on the detector and therefore also increases the overall noise power spectral density, but the optical signal rises faster than the noise.

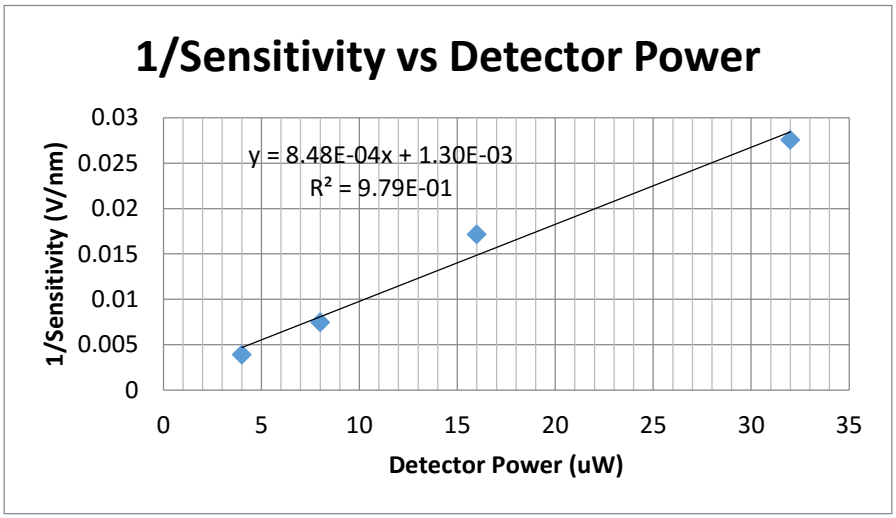

Figure 23: Sensitivity of the improved beam deflection system as a function of optical power hitting the photodetector. The sensitivity of the detection system (nm/V) is inversely proportional to the optical power hitting the photodetector.

be modeled as a function of the power P_D, as shown in Equation (13).

$$D_{SD} = \frac{\beta\sqrt{2q\alpha P_D R^2 G^2 + N_{system}^2 G^2}}{P_D} \tag{13}$$

Figure 24 shows measurements of the deflection spectral density (D_{SD}) as a function of the voltage signal coming from the photodetector (voltage signal is proportional to the optical power P_D hitting the photodetector). At a photodetector voltage of 4 V, D_{SD} was measured to be 3.66e-13 m/√Hz compared to a previous value of 2.5e-12 m/√Hz with the old LED.

Measured AFM System Noise in the Presence of Tip Sample Interaction

The ability to detect a single spin depends upon whether the experimental AFM frequency shift noise is smaller than the predicted frequency shift noise for the on and off resonance cases. The AFM system noise was carefully measured at room temperature as a function of tip sample gap, bias voltage and cantilever oscillation amplitude for comparison with properly scaled simulation data.

To measure the AFM system noise, a 15 nm oxide was thermally grown on a standard silicon AFM tip.[7] The cantilever was then back-coated with aluminum in order to increase its reflectivity. The oxide thickness on the tip was estimated by simultaneously growing an oxide on a planar silicon wafer and measuring it with an ellipsometer. The sample oxide was also thermally grown and measured with the ellipsometer to have a thickness of 10 nm. The tip and sample were cleaned in the UHV AFM chamber using a heat treatment of 600 C for 1 hour for the sample and 250 C for 12 hours for the probe tip.

The AFM probe tip was oscillated (10 nm oscillation amplitude) at its resonance

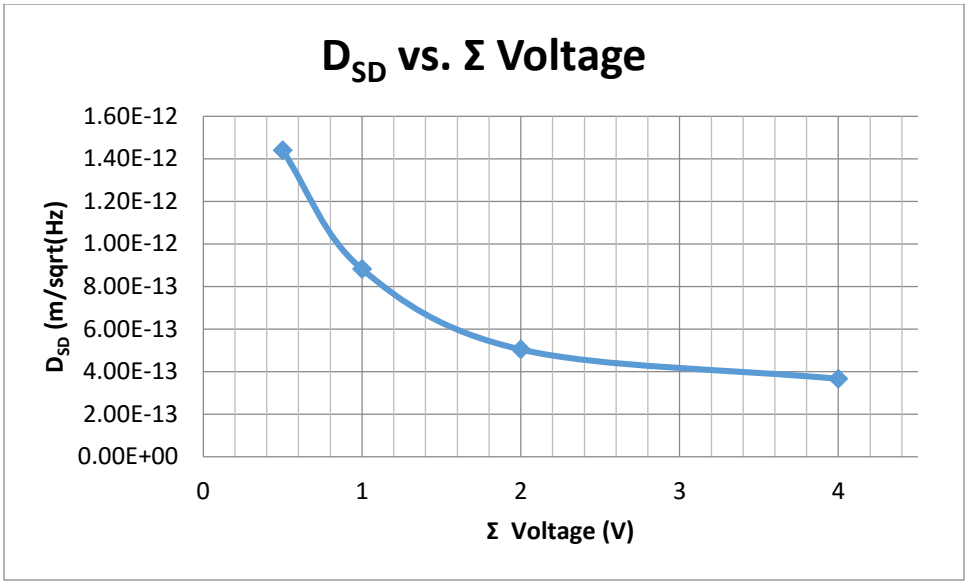

Figure 24: Deflection spectral density vs. photodetector Σ voltage. The deflection noise spectral density (m/√Hz) is found by combining the voltage noise spectral density from the photodetector and the cantilever sensitivity of the OBD system.

frequency (~300 kHz) and brought within a few nanometers of a sample oxide surface. Frequency shift vs. height curves df (z) were then performed in order to establish the proximity with the surface. The oscillation amplitude of the cantilever and the dissipation signal were simultaneously recorded along with the df (z) signal. These measurements were made without any height feedback.

The power spectral density (PSD) of the frequency shift noise, as a function of applied voltage and gap, was measured using a spectrum analyzer. The PSD of the measured noise was post analyzed (integrated) to extract the RMS of the system noise on the cantilever frequency shift as a function of detection bandwidth.

The vacuum gap is a critical parameter in calculating the change in frequency shift associated with the tunneling of an electron to the sample state. The damping and amplitude channels are used to determine the tip-sample contact point. Figure 25 shows a

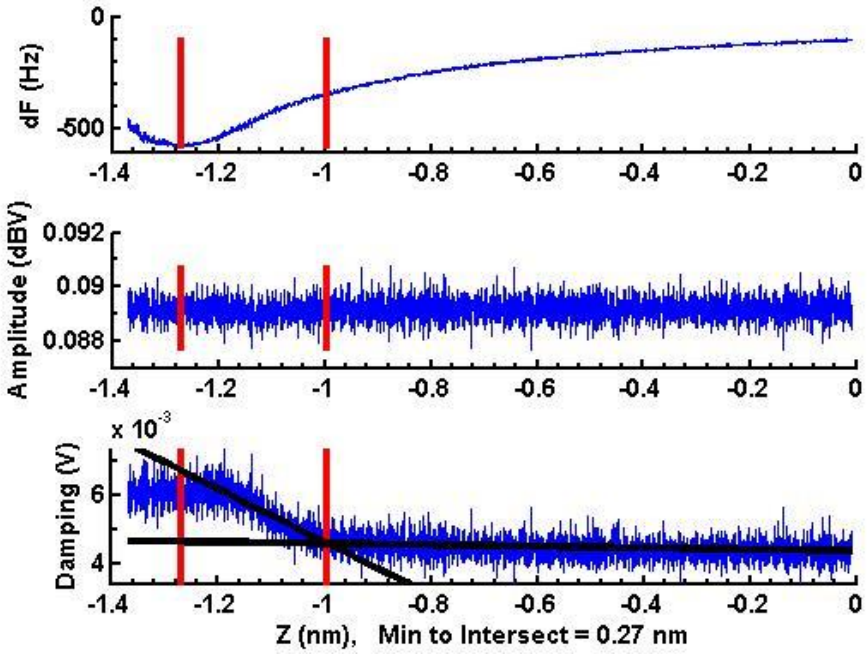

Figure 25: Measuring the gap. Measured AFM frequency shift, amplitude and damping signals vs. tip-sample gap. The increase in the dissipation signal is attributed to the apex of the probe tip making first contact with the surface of the sample.

typical df(z) curve, along with the corresponding dissipation and oscillation amplitude data as a function of gap (z). As the tip approaches the sample surface, the dissipation signal remains constant even in the presence of changing frequency shift, as expected. At approximately 0.3 nm from the df(z) minimum, the dissipation signal sharply increases. This sharp increase in the dissipation signal is attributed to the apex of the probe making significant repulsive contact with the sample surface, causing the dissipation signal to increase sharply.[8] To characterize the system noise, the power spectral density of the df signal was measured as a function of the average cantilever frequency shift. The df(z) curve was then used to determine the tip sample gap, using the contact point determined by the dissipation signal.

Comparison of Theory and Experiment

A comparison is made of the experimentally measured AFM frequency noise data and the theoretical frequency shift data. The theoretical frequency shift data comes from scaling the simulation results with the frequency shift calculated from the electrostatic model (Chapter 3). Previous calculations were performed[9] to show that the average tunneling rate is adequately high ($T_t << T_1 << T_{flip}$) for the depth of states used in the simulations (0.2 nm) at the tip-sample gaps at which the AFM frequency noise measurements were made.

The results of these simulations are displayed in Figure 26. Panel (a) displays the results of these simulations for two rf frequencies corresponding to off- (red) and on- (blue) magnetic resonance cases. In this plot, the simulated RMS of the tunneling noise was converted to a frequency shift (Hz) using the electrostatic calculation described in Chapter 3. While these data where obtained for realistic simulation parameters, they did not account for the presence of system noise found in an actual AFM, which must be appropriately taken into account for realistic comparison. The black data points, taken at various tip-sample gaps, represent experimentally measured room temperature AFM frequency shift system noise as a function of detection bandwidth for a modified commercial scanning probe microscope (Omicron AFM/STM S). The measurements were taken with an applied voltage of 10 volts and consequently, the obtainable energy shift Δ between two states are calculated and shown in Figure 26(a). For larger detection bandwidths, the AFM system noise exceeds the simulated on-magnetic resonance frequency shift noise and even approaches the simulated off-magnetic resonance frequency shift noise. Similarly, as seen from Figure 26(a), at very small bandwidth, the system noise leads to a detectability loss of the magnetic resonance signal. However, for the given

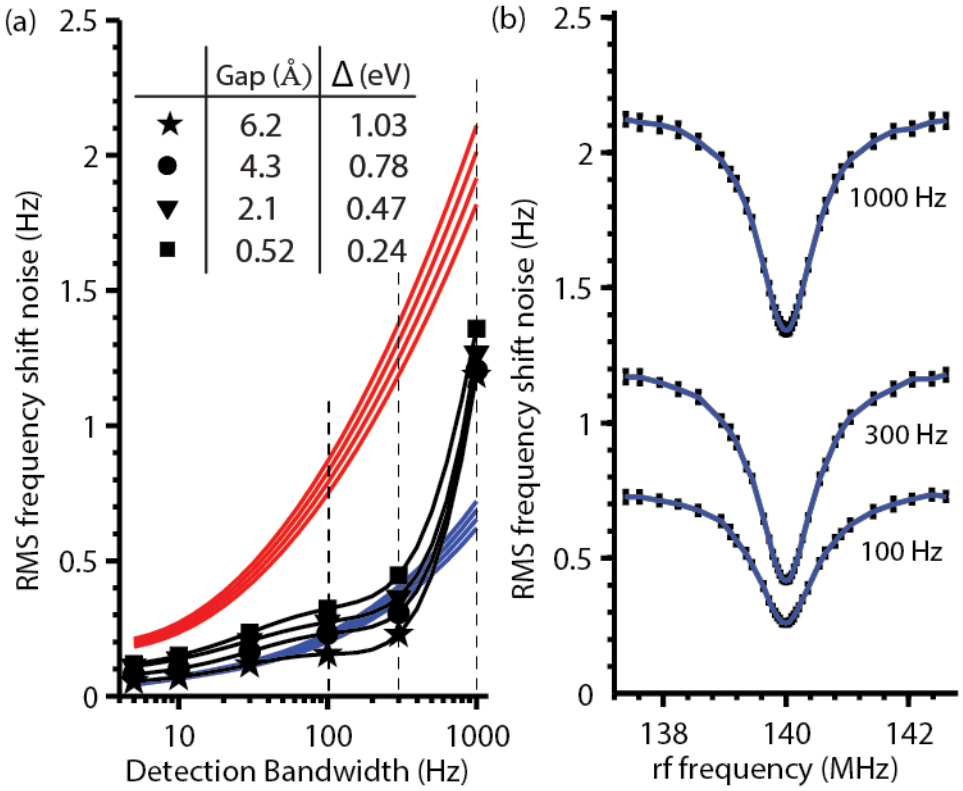

Figure 26: Signal to noise including system noise. Simulated frequency shift noise (RMS) caused by a tunneling RTS in the presence (blue) and absence (red) of magnetic resonance and measured system frequency shift noise (black symbols) connected by a guide to the eye (black line). All data where obtained for four different tip-sample gaps. The table shows the energy shift Δ (eV) of the probe and test state produced by an applied voltage of 10 volts at different tip-sample gaps. (b) Plot of the total frequency shift noise (RMS) consisting of simulated tunneling RTS and the experimentally measured system noise levels as functions of the applied rf frequency for three bandwidth regimes at a tip-sample gap of 0.62 nm. For the assumed constant magnetic field of 5 mT, the rf frequency range covers the g=2 electron spin resonance condition. The error bars indicate the standard deviation of the simulated RMS of the tunneling noise and measured noise power for an integration time of 1000 ms. In order to discriminate on- from off-magnetic resonance conditions needed for the single-spin detection, the on resonance RMS of the tunneling noise and the system noise need to be significantly lower than the off resonance RMS of the tunneling noise. This condition is fulfilled between ≈10 Hz and ≈1 kHz bandwidth.

simulation parameters and the measured noise data, there is a bandwidth range between $f \approx 10$ Hz and 1 kHz in which the system noise is significantly lower than the simulated off-magnetic resonance frequency shift noise. Hence, for the given spin lattice relaxation and tunneling parameters, the given scanning probe setup and bandwidths, force detected single-spin magnetic resonance detection becomes possible at room temperature.

In a single-spin detection experiment, the frequency of the applied rf magnetic field is swept through magnetic resonance. Figure 26(b) shows how the frequency shift noise due to spin dependent tunneling as a function of the frequency of an applied rf field can reveal magnetic resonance of a single spin, in the presence of real AFM system noise. In these calculations, the RMS of the AFM system noise power has been appropriately added to the tunneling RTS frequency shift noise (assuming it is uncorrelated, i.e., sum of the squares). The error bars in these plots represent the standard deviation of the RMS of the tunneling noise obtained from multiple simulations of 1000 ms length and calculated variations of measured experimental noise, assuming Gaussian statistics. The standard deviation of the AFM system noise amplitude was obtained by simulating a Gaussian noise power spectrum which was matched to the measured value of the AFM system noise measurements.

Figure 27 illustrates the effect of performing these measurements at different frequency scan rates. Figure 27(a) and (b) show the expected magnetic resonance curves for a 100 and 10 ms measurement time per frequency step, respectively. These curves can be compared with the results shown in Figure 26(b), which assumes a 1 second measurement time per frequency step. As the time per point is reduced, the standard deviation in the RMS of the tunneling noise becomes larger. The blue curves in

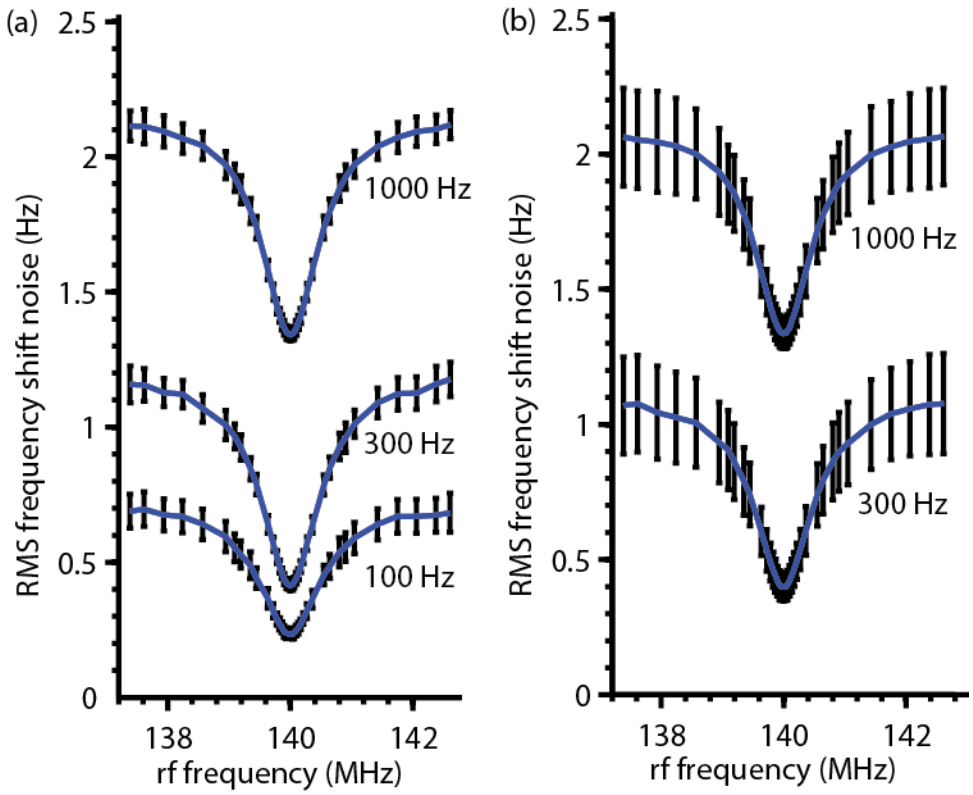

Figure 27: Magnetic resonance response with system noise vs. acquisition time. (a) Total frequency shift noise, including both simulation and AFM system noise for three different bandwidths (1000 Hz, 300 Hz, and 100 Hz) and as a function of rf frequency. This data is produced for a simulation time of 100 ms per point. The error bars include statistical fluctuations due to the standard deviation of the simulation noise and the calculated standard deviation of the measured AFM system noise. (b) Same as in (a) but with a simulation time of 10 ms per frequency step with 2 bandwidths (1000 Hz and 300 Hz).

Figure 27(a) and (b) represent the sum of the simulation signal noise and the AFM system noise (assumed to be uncorrelated) as a function of rf frequency, for the largest tip-sample gap (6.2 Angstroms). They represent the average RMS of the tunneling noise calculated from many separate simulations, each having a total simulation time of 100 ms for Figure 27(a) and 10 ms for Figure 27(b). The error bars on the blue resonance curves represent the sum of the statistical fluctuations that occur from simulation to simulation and the calculated statistical fluctuations of the measured AFM system noise. The statistical fluctuations of the AFM system noise were simulated using a Gaussian noise power

spectrum which was matched to the measured AFM noise measurements.

Figure 27(a) shows that the spin signature can be clearly detected with a 1000 Hz bandwidth and a finite signal to noise ratio when the rf frequency is swept at a rate of 100 ms per frequency step. For smaller detection bandwidths, the S/N ratio decreases.

Figure 27(b) was simulated with a total acquisition time of 10 ms per frequency step and shows that the resonance dip is near the detection limit for a bandwidth of 300 Hz. The three data sets were calculated based upon AFM system noise measurements obtained at room temperature and show the detectability of magnetic resonance for several detection bandwidths.

References

1. K. Ambel, A. Payne, C. Williams, and C. Boehme, (arxiv: cond-mat: 1310.0094 2013).

2. K. E. Yokogawa, Y. Yajima, T. Mizutani, S. Nishimatsu, and K. Suzuki, Jpn. J. Appl. Phys. **29**, 2265 (1990).

3. M. E. Zvanut, R. E. Stahlbush, and W. E. Carlos, Appl. Phys. Lett. **60**, 2989 (1992).

4. Y. Ishikawa, M. Okigawa, S. Samukawa, and S. Yamasaki, J. Vac. Sci. Technol. B **23**, 389 (2005).

5. Y. Ichihashi, Y. Ishikawa, Y. Kato, R. Shimizu, M. Okigawa, and S. Samukawa, Jpn. J. Appl. Phys. **45**, 8370 (2006).

6. S. Torbrügge, J. Lübbe, L. Tröger, M. Cranney, T. Eguchi, Y. Hasegawa, and M. Reichling, Rev. Sci. Instrum. **79**, 083701 (2008).

7. Nanosensors^{TM}, Type PPP-NCH.

8. N. Oyabu, P. Pou, Y. Sugimoto, P. Jelinek, M. Abe, S. Morita, R. Perez, and O. Custance, Phys. Rev. Lett. **96**, 106101 (2006).

9. N. Zheng, C. C. Williams, E. G. Mishchenko, and E. Bussmann, J. Appl. Phys. **101**, 093702 (2007).

CHAPTER 5

OBSERVED RANDOM TELEGRAPH SIGNAL

Experimental Efforts to Identify a Tunneling RTS Signal

Before the proposed magnetic resonance measurement can be performed, an appropriate tunneling RTS signal must be observed and verified. In order to carry out experiments to produce a tunneling RTS, the oxidized AFM probes were brought within tunneling range of the oxide sample described in Chapter 4, and a discrete two-level signal was observed on the frequency shift of the AFM. This provided optimism for attempting to perform the magnetic resonance experiment.

First Attempt at Single-Spin Experiment

Figure 28 shows the results from a first attempt at the single-spin experiment. Each data point represents the RMS frequency shift noise df as a function of rf frequency. At each frequency step, a frequency shift noise time trace is acquired and then corrected by subtracting any background slope and offset. The root-mean-square of the df amplitude is then calculated for each of these background subtracted df time traces.

The absence of any spin resonance signature, motivated a careful investigation into how the entire experiment had been implemented. One of the most important evaluations was to test for the observed RTS signal against a tunneling model and developing a criterion for identifying suitable paramagnetic states.

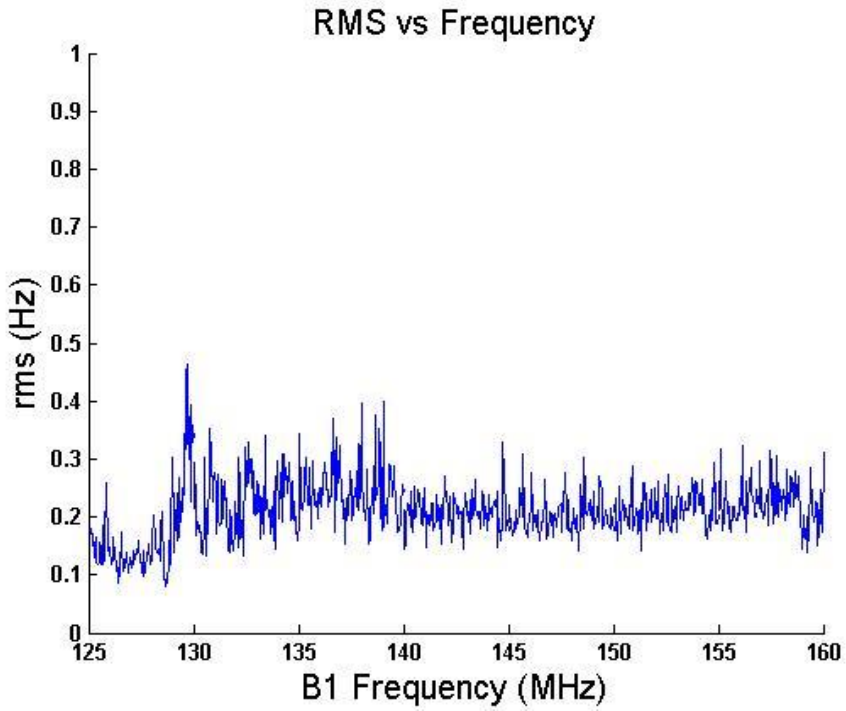

Figure 28: Experimental RMS of the frequency shift noise vs. rf frequency sweep.

Constant Height Measurements of Oxide-Oxide Binary Signal

The AFM tip is carefully brought within tunneling range of a high E' density sample ($10^{18}/cm^3$) without any height feedback. When the tip-sample gap is sufficiently small, a discrete two-level random telegraph signal occasionally appears on the df signal channel. This is shown in Figure 29.

The red curve is an RTS signal obtained without any height control feedback (nominally constant height trace of df vs. time). This RTS signal has a slight linear slope (blue line) which is attributable to thermal drift of the tip relative to the surface. The green curve is a 2 nm height scan (tip moves 2 nm towards the surface, and then moves 2 nm away from the surface) that was performed moments before the constant height trace. The green curve is helpful in identifying the attractive and repulsive regions and in approximating the absolute distance of the probe from the surface.

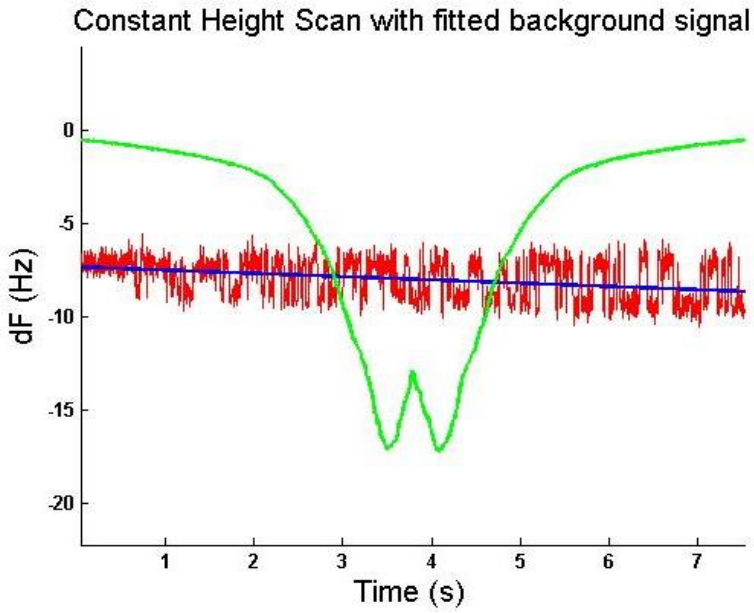

Figure 29: Random telegraph signal (raw data) seen on the cantilever frequency shift df. This signal comes from an oxidized tip being brought within tunneling range of an oxidized sample. Constant height scan (red curve) with 2 nm height scan (green line) to show proximity to sample surface.

Figure 30 is a histogram of the observed RTS signal vs. df, after background slope removal and digital filtering. It clearly shows the two-level nature of this observed RTS signal. 0 Hz on the histogram is referenced to the average frequency shift fit (blue line) to the data shown in Figure 29.

At the core of the single electron spin detection approach is the detection of a random telegraph signal (RTS) by the AFM cantilever. The observed RTS signal in Figure 29 ideally corresponds to an electron tunneling back and forth between two localized paramagnetic states, one in the tip oxide and one in the sample oxide. As the states in the tip and sample are brought close together (within tunneling range), the tunneling rate is set by the overlap of the wave functions of the two states. This overlap is dependent upon the tunneling barrier height. If the barrier height is near 5 eV, the expected tunneling rate should increase approximately by an order of magnitude per Angstrom change in tip-

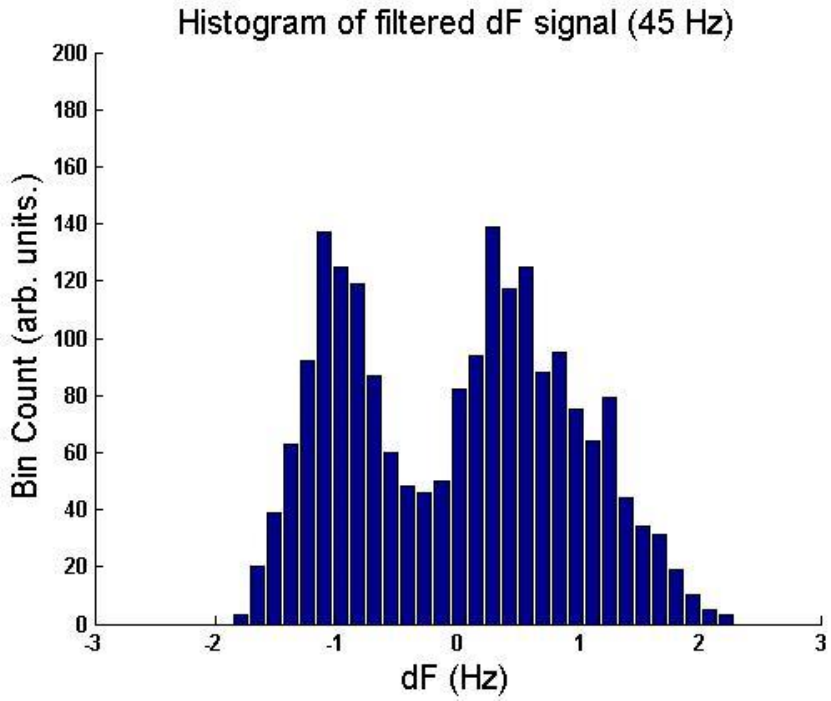

Figure 30: Potential RTS histogram. Background subtracted df data (from Figure 29) showing a potential RTS signal is displayed through a histogram to show the discrete two level system.

sample gap.[1] The measurement of how the tunneling rate changes as the tip-sample gap changes provides the information needed to determine the actual tunneling barrier height between the two states.

A second criteria for the elastic tunneling experiment is that the energy of one state, when occupied by a single electron, must be the same as the energy of the other paramagnetic state when occupied by two electrons (in a singlet state). In other words, the energies of the defect states must differ by the coulomb energy associated with the addition of one electron to the other state. The singly occupied state and the doubly occupied state can be energetically aligned using a voltage bias between the tip and sample as described in Chapter 2.

Thus, the barrier height and the relative energy of the two paramagnetic states

provide a signature for states useful in the proposed methodology. For a particular pair of states to be a candidate for performing the proposed single electron spin detection measurement, they should behave with an appropriate gap dependence (barrier height) and appropriate voltage dependence (energy relationship).

RTS Frequency Dependence on Tip-Sample Gap

The frequency of the RTS signal should be dependent on the tip sample gap. As the gap is made smaller, the respective electron wave functions in the tip and sample should have greater overlap, and the probability of tunneling should increase. Therefore, reducing the gap should increase the average frequency of the RTS signal.

Experiments were done to verify the gap dependence on the RTS frequency. An oxide tip and an oxide sample were carefully brought within a few nanometers of each other. A 2 nm height ramp was first performed in order to verify the proximity of the sample surface. Subsequently, without any height control feedback, the gap was manually decreased in 0.2 Angstrom steps. If no RTS signal was detected, the scan was aborted and a new location was chosen. For one particular location, Figure 31 shows all the recorded constant height scans as well as the 2 nm height ramp to show their relative height to each other and the sample surface.

Figure 32 shows each separate height scan with the background subtracted and digitally filtered. Each has an arbitrary offset in order to view them clearly on the same graph. Starting from the top, each subsequent scan represents a decrease in gap by 0.2 Angstroms. From the top blue scan (-50 Hz) to the subsequent green scan, there is a decrease in the telegraph frequency even though the gap decreased. The subsequent red scan then shows an increase in the telegraph frequency which is consistent with the

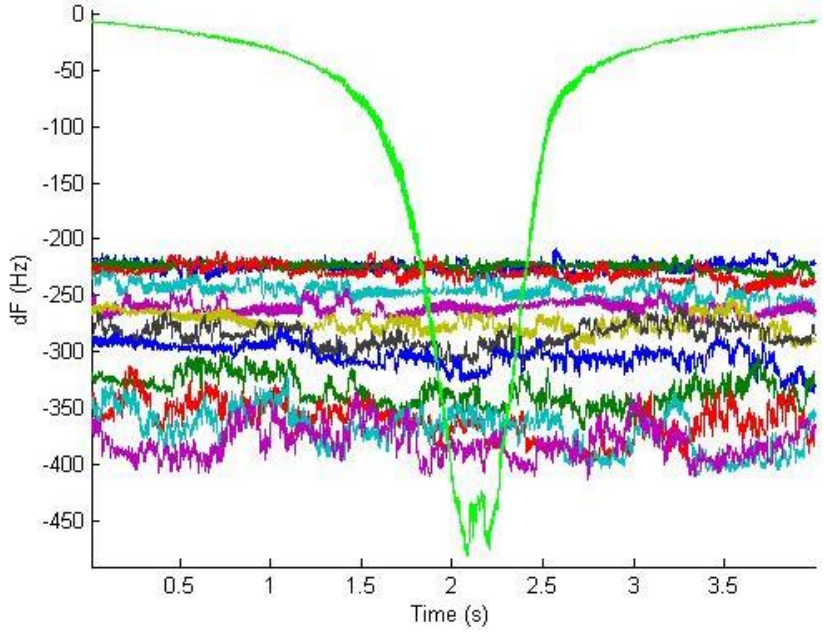

Figure 31: Multiple frequency shift df vs. time traces taken at different heights. A 2 nm height ramp (green line) shows the proximity to the sample surface.

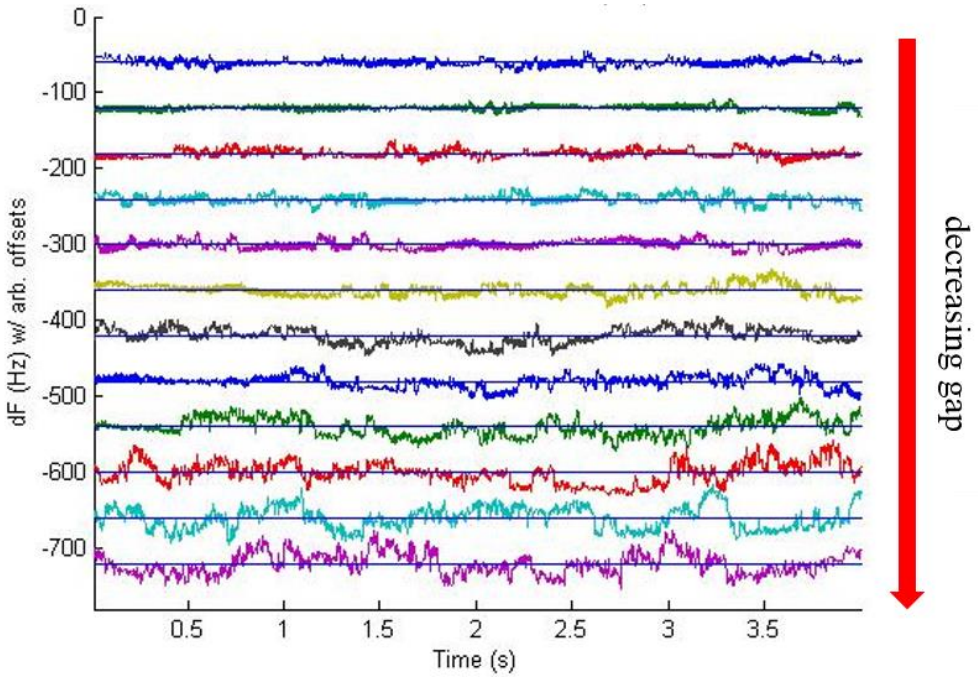

Figure 32: RTS height dependence scans. This experiment is meant to show the height dependence on the RTS frequency. The data sets from Figure 31 have been offset to see how the frequency of the binary steps correlate with the tip sample gap. The lack of correlation points to the idea that this signal is not due to electron tunneling events between two paramagnetic defect states.

decrease in gap.

Looking at this collection of scans as a whole, there does not appear to be a strong correlation between a decreasing gap and an increasing RTS frequency. Other measurements conducted at different locations also failed to produce a clear correlation between a decreasing gap and an increasing RTS frequency. These measurements raised questions about whether the random telegraph signal was due to single electron tunneling between two defect states.

RTS Tunneling Dependence on Applied Voltage

A voltage dependent RTS that shows the proper energy relationship between two paramagnetic states signifies that the states involved are good candidates for the single-spin resonance experiment. The purpose of the applied voltage ramp is to continuously scan the energy of the state in the tip oxide relative to states in the sample oxide surface. This spectroscopic measurement would show whether the RTS signal is voltage dependent. The RTS signal should "turn on" when the states are energetically aligned and "turn off" when the states are not aligned.

Experiments have been performed to ascertain whether the observed RTS tunneling behaves as expected (voltage dependence) at various tip sample gaps. An oxidized tip is positioned near an oxide surface with height feedback on for some time to eliminate tip/sample drift. The height feedback is then turned off, and a voltage ramp is applied between the tip and sample. This experiment is repeated at several probe tip heights, so that when the states are aligned, the tunneling rate would be measurably different.

Figure 33 shows the measured cantilever frequency shift vs. probe tip–sample gap (df (z)) with the largest negative frequency shift (far left) corresponding to the tip being

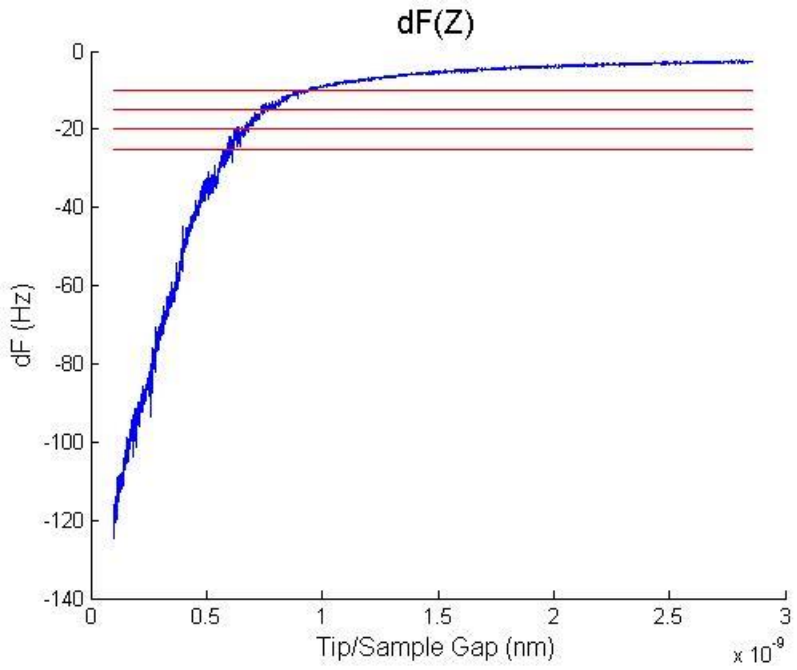

Figure 33: df(z) curve for df(v) spectroscopy. Frequency shift curve (df (z)) with red horizontal lines showing frequency shifts and heights at which the frequency shift vs. voltage curves (df(v)) were acquired, shown in Figure 34.

within ~ 0.1 nm of the surface. The red horizontal lines show the different heights at which the voltage ramps were performed and data acquired. The df signal is collected while the applied voltage is ramped from 10 to +10 volts. The data is post processed to remove a parabolic background on the df signal. This background subtraction is done separately for each voltage ramp. The corresponding frequency shift at zero applied voltage (relative to the flatband condition) is shown to the right of each scan in Hertz. These frequency setpoints (shown as red lines in Figure 33) correspond to the probe tip heights established by the df(z) curve in Figure 33.

From Figure 34, one can see that the voltage ramps performed far from the surface (i.e., -10 Hz setpoint) do not show any RTS noise. In that case, the probe tip is decoupled from the surface and the only noise observed is the UHV AFM system noise. When the tip is positioned closer to the surface (i.e., -15, -20 and -25 Hz setpoints, corresponding to

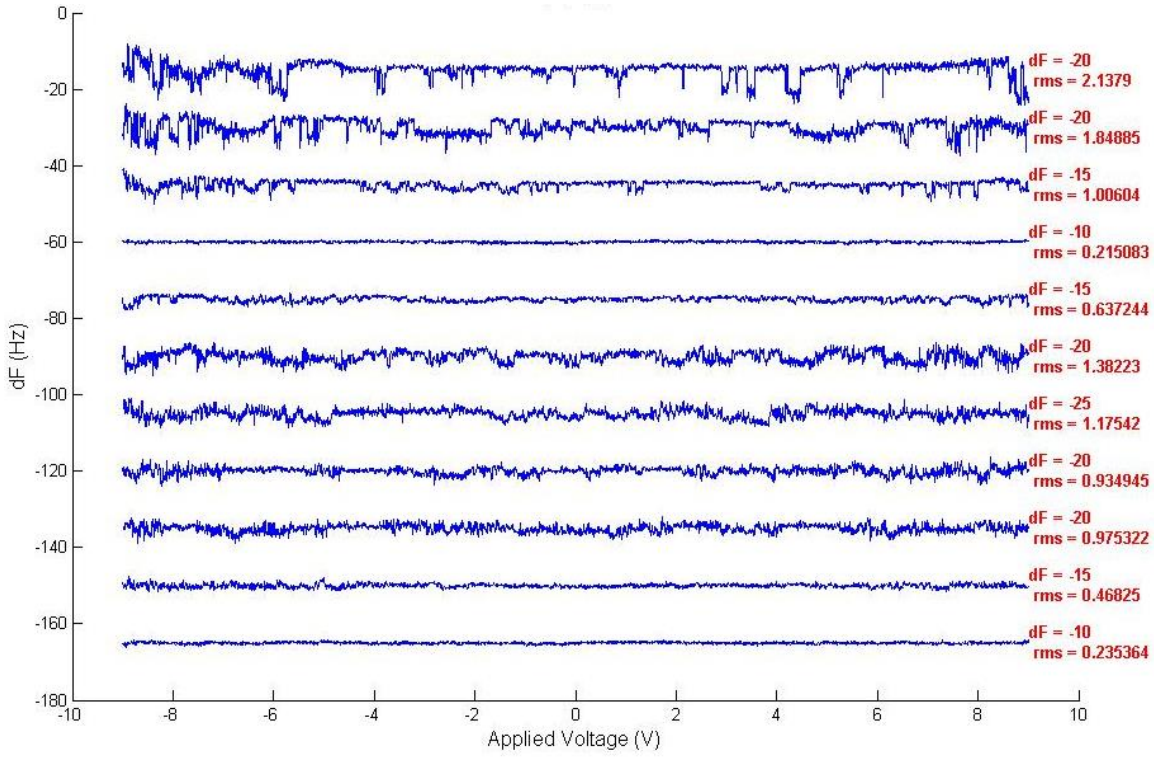

Figure 34: df(v) of RTS signal at several gaps. Background subtracted frequency shift vs. voltage curves (df(v)) taken at various heights for an oxide sample and an oxide probe tip. A quadratic background has been subtracted from each trace. The data on the far right provides the average frequency shift (in Hertz), which can be used to determine the probe height, using the data shown in Figure 33. It also provides the RMS value of the voltage trace. Because the RTS signal does not appear to systematically depend on voltage, the signal is not likely due to electron tunneling between two paramagnetic states.

tip-sample gaps of approximately 0.7 nm, 0.6 nm, and 0.5 nm gap respectively) a random telegraph signal is observed throughout the entire voltage ramp.

The actual voltage between the tip and sample is smaller than the applied voltage and depends upon the tip sample gap. For the smallest gap (-25 Hz setpoint, 0.5 nm gap), the estimated voltage drop between tip oxide surface and sample oxide surface (actual movement of the energy of the tip states relative to the sample states) is ± 0.75 V (± 0.75 eV) above and below the flatband condition. For the largest gap (-10 Hz setpoint, 0.8 nm gap), the estimated voltage drop in the gap is ± 1.13 V (or ± 1.13 eV relative movement of

the tip and sample states). Note that this movement is much bigger than kT (~25 meV at room temperature). Therefore, we would expect in these datasets that the random tunneling would "turn on" and "turn off" as the energy of the two participating trap states move with respect to one another. The experimental parameters used to calculate the voltage dropped in the gap in this case are: sample oxide thickness = 10 nm and tip oxide thickness = 15 nm. These observations of the RTS signal being independent from an applied voltage are not consistent with states useful for performing the single-spin detection experiment.

In summary, the data shown in Figure 32 and Figure 34 do not show the expected height and voltage dependence on the tunneling rate. While it is unclear what physical phenomenon is producing this binary state signal, these measurements do not behave with the voltage and gap dependence expected from the simple picture of a single electron tunneling between two electron trap states.

There are some additional observations that are surprising. If an oxide covered tip is brought near an oxide surface, a RTS is observed on the order of 30% of the time. This is surprising, given that the expected density of the native trap states in the oxides is relatively low. EPR measurements[2] performed on thermally grown silicon dioxide films have shown E' center defect densities in the range of $10^{15}/cm^3$. This means that on average there is only one trap state per $(100\ nm)^3$. This is the reason that a method was developed to create E' centers at high density.[2] The observation that 30% of the time an RTS is observed is well above than expected. Of course, these measurements are difficult because every tip has its own behavior and every location on the surface is different. Over days, the surface typically becomes "dirty," due to the addition of adsorbates from the vacuum, which is maintained at a pressure of ~ 10^{-10} Torr. Surface contamination introduces

uncertainty as to what is going on between tip and sample.

To eliminate the possibility that molecules were jumping back and forth between the tip and surface oxides, a calculation was done to determine what frequency shift a single molecule could induce on the tip. The result showed that a single molecule could not possibly introduce a frequency shift on the order of a few Hertz, as observed in the actual RTS measurements. The frequency shift from a single molecule would be a factor of 10^6 too small.

So, where could the RTS come from? Recent considerations have pointed toward chemical bonding events that might be occurring between tip and sample oxide surfaces. If the surface of the oxide has unterminated or dangling bonds, then as the probe tip is brought closer to the sample surface, the atoms or molecules at either surface could chemically attach to or detach from the atoms or molecules of the other surface.[3, 4] Baytekin et al. showed chemical modifications of two dielectric surfaces when they came in contact with each other by means of material transfer as well as contact charging.[5] Another possibility could be the motion of a bistable atomic or molecular defect within the tip sample region.[6] If an atom or defect has two configurations separated by an energy barrier, the finite temperature could cause the atom or defect to randomly fluctuate between these two sites. The defect or atom could be very close to the apex of the tip. These phenomena could happen on the scale of fractions of a second (could be metastable). The resultant frequency shift could look like a RTS.

These possibilities could explain the occurrence of the observed RTS. Such phenomena do not preclude the possibility of tunneling between trap states, but if their occurrence is much more prevalent, they could mask such tunneling events. These are a

few possibilities that explain the observations in this experiment.

Conclusion

There are still significant challenges that need to be overcome before the experimental realization of the proposed single-spin detection experiment. One important challenge is that of producing a probe tip with a paramagnetic state at the very apex. The existence of a defect state at the end of a probe tip could be independently verified by approaching the tip to a clean metal surface and changing the occupancy of the defect state by changing the Fermi level of the tip with an applied voltage. Such electron manipulation should be reproducible and should occur at all locations of the clean metal sample. Once this tip characterization has taken place, identifying a tunneling RTS signal with the same tip on an oxide sample could be pursued and the results could be more easily interpreted.

In conclusion, this work has provided a theoretical feasibility study of a scanning probe based single-spin detection scheme with the potential for atomic scale spatial resolution. A simulation was created to show the tunneling dynamics of a single electron tunneling between two paramagnetic states. This simulation identified the RMS of the tunneling noise as a suitable observable. The simulation was then converted into an AFM cantilever frequency shift by means of a one dimensional electrostatic model. These scaled simulation results were then compared against experimentally measured values of a commercial AFM's system noise in the presence of tip sample interaction. The comparison showed that single-spin detection should be achievable at room temperature. The experimental details of the AFM system improvements were also discussed. Finally, measured RTS signals were analyzed. The results of this analysis showed that the observed

RTS signals are not likely due to the tunneling phenomenon needed to demonstrate the single-spin method.

References

1. N. Zheng, C. C. Williams, E. G. Mishchenko, and E. Bussmann, J. Appl. Phys. **101**, 093702 (2007).

2. K. Ambel, A. Payne, C. Williams, and C. Boehme, (arxiv: cond-mat: 1310.0094 2013).

3. S. Kawai, T. Glatzel, B. Such, S. Koch, A. Baratoff, and E. Meyer, Phys. Rev. B **86**, 245419 (2012).

4. A. L. Shluger, L. N. Kantorovich, A. I. Livshits, and M. J. Gillan, Phys. Rev. B **56**, 15332 (1997).

5. H. T. Baytekin, A. Z. Patashinski, M. Branicki, B. Baytekin, S. Soh, and B. A. Grzybowski, Science **333**, 308 (2011).

6. P. M. Hoffmann, S. Jeffery, J. B. Pethica, H. Özgür Özer, and A. Oral, Physical Rev. Lett. **87**, 265502 (2001).